Journal of Computational Physics 422 (2020) 109766

Contents lists available at ScienceDirect

Journal of Computational Physics

www.elsevier.com/locate/jcp

High order central WENO-Implicit-Explicit Runge Kutta schemes for the BGK model on general polygonal meshes

Walter Boscheri [a,b], Giacomo Dimarco [a,b,*]

[a] Department of Mathematics and Computer Science, University of Ferrara, Via Machiavelli 30, 44121 Ferrara, Italy
[b] Center for Modeling, Computing and Statistic CMCS, University of Ferrara, Via Muratori 9, 44121 Ferrara, Italy

ARTICLE INFO

Article history:
Received 20 August 2019
Received in revised form 26 June 2020
Accepted 10 August 2020
Available online 18 August 2020

Keywords:
Kinetic equations
Finite volume
Central WENO reconstruction
Implicit-Explicit Runge Kutta
Unstructured meshes
High performance computing

ABSTRACT

In this work, a family of high order accurate Central Weighted ENO (CWENO) finite volume schemes for the solution of nonlinear kinetic equation of relaxation type is presented. After discretization of the velocity space by using a discrete ordinate approach, the space reconstruction is realized by integration over conformal arbitrary shaped closed space control volumes in a CWENO fashion. Compared to other WENO methods on unstructured meshes, in the method here presented, the total stencil size is the minimum possible and the linear weights can be arbitrarily chosen. These two aspects make their use for kinetic equations and the practical implementation on general unstructured meshes particularly interesting. The full discretization is then obtained by combining the previous phase-space approximation with an Implicit-Explicit Runge Kutta high order time discretization which guarantees stability, accuracy and preservation of the asymptotic state. In particular, to guarantee in the finite volume framework space accuracy higher than two, a new class of IMEX methods has been set into place and its properties have been studied. The formal order of accuracy is numerically measured for different regimes, computational performances of the proposed class of methods are tested on several standard two dimensional benchmark problems for kinetic equations. The novel methods are finally applied to a prototype engineering problem consisting in a supersonic flow around a NACA 0012 airfoil. In our computations we employ up to ≈ 325 millions of degrees of freedom and 256 GB of RAM run on 128 cores with `Fortran`-MPI providing evidence that the above schemes are suitable for implementation on parallel distributed memory supercomputers.

1. Introduction

Kinetic models provide a description of systems of interacting particles at different regimes [10,18]. This description of a gas relies on an equation for the time evolution of the so-called probability distribution function. This gives the probability for a particle to be at a given position, with a given velocity, at a fixed instant of time. Consequently, the full problem depends, in general case, on seven independent variables: three for the space, three for the velocity plus the time. On one hand, if this approach permits to detail a richer set of physical phenomena, on the other hand it makes difficult the realization of numerical simulations due to the well-known curse of dimensionality issue.

* Corresponding author.
E-mail addresses: walter.boscheri@unife.it (W. Boscheri), giacomo.dimarco@unife.it (G. Dimarco).

https://doi.org/10.1016/j.jcp.2020.109766
0021-9991/

The problem of the excessive computational cost can be overcome, at least in some situations, by probabilistic methods [10,17,80]. In fact, for steady state problems, the possibility to take time averages of the solution allows the computational cost to be reduced, especially in the multidimensional cases, while maintaining a reasonable accuracy. This, unfortunately, does not hold true anymore for unsteady problems, even if some remedies have been studied in the past [4,38,39,33].

Another strategy which has been shown to be able to deal efficiently with multidimensional kinetic equations has been recently proposed in [34–36]. This methodology is based on a Lagrangian technique [20,50,58,28,27] which exactly solves the transport step, and on a projection step to compute the collision term. This scheme has been successfully employed to compute the solution of a full six dimensional relaxation type kinetic equation. These simulations were run on a single core machine in a reasonable amount of time at least for small mesh sizes. In [37] also the full Boltzmann equation in the six dimensional space has been solved relying on the same scheme in synergy with spectral methods for the Boltzmann operator and high performance parallel computers. However that method, even if very efficient, exhibits limitations in term of spatial accuracy being the order of convergence restricted to one. Moreover, it presents limits in term of versatility being based on a regular Cartesian mesh.

In this work, we follow an alternative path and we pursue a direction which permits to have both high order accuracy in space-time and an excellent versatility of the numerical scheme to deal with different geometries due to the unstructured property on which the method is based on. The price we pay lies in the computational cost compared to [34]. We deal with three different levels of discretization of the underlying kinetic equation: discretization of the velocity space, discretization of the physical space and time discretization. For each of these variables, we choose a different strategy. As a first step, a classical discrete velocity, or discrete ordinate, models (DVM) approach [11,82,85] replaces the continuous kinetic model. The DVM models are obtained by discretizing the velocity space into a set of fixed discrete velocities [11,78,82,81]. As a result of this step, one has to deal with a finite set of linear transport equations with a source term which couples all the equations together. This source term describes the collisions or, more in general, the interactions between the particles. The necessity to truncate the infinite velocity space and to set a finite number of points in this space brings drawbacks from the numerical point of view [11,78,56,79] which will be discussed later.

In order to solve the transport part of the DVM model, many different techniques can be employed like finite difference, finite volume or semi-Lagrangian methods [52,78,29,77,64,94,95,90,91,84,58]. Here, we follow a finite volume strategy and we restrict our study to the relaxation approximation of the Boltzmann equation known as the BGK model [9]. In a finite volume approach, one stores and evolves the so-called cell averages of the distribution function on a computational grid. Entering into details, the high order space accuracy we ask for requires more spatial information. Classically, they are obtained by a reconstruction that produces high order piecewise polynomials from the known cell averages in an appropriate neighborhood of the control volume under consideration. Many reconstruction strategies exist, we recall the famous Weighted Essentially Non Oscillatory reconstruction (WENO) [66,21,88]. This interpolation method is rather simple and very efficient in the one-dimensional case and easily extends to multiple space dimensions if uniform Cartesian meshes are employed [92,49]. On unstructured meshes, however, high order reconstructions are less simple and we recall some pioneering works on this subject intended to face this problem [7,6,1] and later improvements [61,48,96]. We also recall two review papers which discuss some recent results on this subject [2] and [65]. The main difficulty in applying the WENO idea to unstructured meshes or to reconstructions at points inside the computational cells comes from the definition of the linear weights (see for instance [70] and [45] for a detailed discussion) and we consequently abandon this idea. In this work, we concentrate instead on a Central WENO reconstruction (CWENO) originally introduced in the context of conservation laws in the one-dimensional case [73], in order to obtain a third-order accurate reconstruction at the cell center that could not be provided by the classical third order WENO scheme. This technique was later developed for non-uniform meshes for instance in [24] and [45]. Here, we extend these techniques to the case of kinetic equations on arbitrarily polygonal conformal meshes and, to the best of our knowledge, this is the first work in this direction.

The third type of discretization, i.e. the time one, is handled by using the so-called Implicit-Explicit Runge-Kutta methods. Kinetic equations are well known to represent a real challenge for numerical methods not only for the curse of dimensionality but also for the different space and time scales involved in their resolution. In particular, close to the fluid limit, the intermolecular collision rate grows exponentially and the collisional time becomes very small, while the fluid dynamic time scale conserves much larger values [18,43]. However, the use of standard implicit approaches, which in principle will be enough to solve the problem, are prohibited by the nonlinearity of the equations as well as by the dimension of the systems that have eventually to be inverted. Several authors have tackled the above problem in the recent past [43,68,69,51,8,25,26,30–32,41,42,40,44,75,76,62,63] by developing and studying the class of methods known as Asymptotic Preserving. These techniques allow the full problem to be solved in the entire domain for all choices of time steps and Knudsen numbers with a time step which is independent from the fast scale identified by the Knudsen number. In this work, we make use in particular of the so-called Implicit-Explicit Runge-Kutta methods [3,83,42] that are able to achieve high order, while maintaining the stability and the asymptotic preserving property. An important remark concerns the use of implicit discretizations in the finite volume context which can not be handled by direct application of the IMEX strategy as done for finite difference methods in [42]. In particular, to solve the problem of inverting the collisional term which cannot be directly done if high order in space has to be guaranteed, we rely on a splitting of the collision operator into a cell average plus a correction term. The first term is treated implicitly, while the small correction is treated explicitly as proposed in [13] in the context of balance laws in the one dimensional case. The Asymptotic Preserving property and the accuracy of this new method are studied.

Summarizing, in this paper we introduce a novel CWENO-IMEX Runge-Kutta high order Asymptotic Preserving class of methods on arbitrarily shaped unstructured grids by reconstructing piecewise polynomials from given cell averages. These methods are successively tested on benchmark multidimensional rarefied gas dynamic problems. The formal accuracy is numerically tested for different regimes. Finally a more realistic test case involving a flow around a NACA 0012 airfoil for different values of the Knudsen number is performed. In order to demonstrate that the methods are also well suited for the implementation on parallel distributed memory supercomputers, a MPI parallelization is realized distributing the space variable on different threads. A profiling of the code is also reported. Alternative type of parallelizations can be explored but we do not consider this possibility here. A computation involving around 10 million cells and 100 million degrees of freedom, namely 6500 control volumes in space and 1600 cells in velocity space at third order in space-time, has been run on 128 cores. Extension of the above method to larger set of degrees of freedom is possible using larger high performance computational resources.

The article is organized as follows. In section 2, we introduce the BGK model, its properties and its fluid dynamic limit. In Section 3, we present the discrete ordinate discretization, including drawbacks and possible solutions. Then, in Section 4, the CWENO reconstruction and a first fully discretized method is shown in detail. In Section 5, the new IMEX Runge-Kutta schemes applied to the phase-space discretization of the kinetic equations are presented and the notion of asymptotic preservation and asymptotic accuracy is recalled. The strategy which permits to achieve high order in time accuracy in the finite volume framework is discussed and some properties of the schemes are also studied in this part. Finally, Section 6 is devoted to present several numerical examples of the schemes obtained up to third order accuracy in space and time, showing the capability of the novel methods to deal with such equations. Conclusions are reported in a final Section together with a discussion on future investigations.

2. Boltzmann-BGK equation

We consider kinetic equations of relaxation type as follows:

$$\partial_t f + v \cdot \nabla_x f = \frac{\nu}{\varepsilon}(M_f - f). \tag{1}$$

This equation supplemented by the initial condition $f(x, v, t = 0) = f_0(x, v)$ furnishes the time evolution of a non negative function $f = f(x, v, t)$ which gives the distribution of particles with velocity $v \in \mathcal{R}^{d_v}$ in the space $x \in \Omega \subset \mathcal{R}^{d_x}$ at time $t > 0$. Equation (1) is the so-called BGK equation or model [9,18]. In this model, the complex interactions between particles are substituted by a relaxation towards the local thermodynamical equilibrium defined by the Maxwellian distribution function M_f

$$M_f = M_f[\rho, u, T](v) = \frac{\rho}{(2\pi\theta)^{d/2}} \exp\left(\frac{-|u - v|^2}{2\theta}\right), \tag{2}$$

where $\rho \in \mathcal{R}$, $\rho > 0$ and $u \in \mathcal{R}^d$ are respectively the density and mean velocity, while $\theta = RT$ with T the temperature of the gas and R the gas constant fixed to $R = 1$ for simplicity. For simplicity, in the description of the method, we do the hypothesis that the dimension of the physical space is the same of the dimension of the velocity space $d_x = d_v = d$. However, the numerical method is not restricted to this particular choice and it is possible to consider different dimensions between the space and the velocity in order to obtain different simplified models.

The macroscopic values ρ, u and T are related to f by

$$\rho = \int_{\mathcal{R}^d} f dv, \qquad u = \frac{1}{\rho}\int_{\mathcal{R}^d} v f dv, \qquad \theta = \frac{1}{\rho d}\int_{\mathcal{R}^d} |v - u|^2 f dv, \tag{3}$$

whereas the energy E is defined by

$$E = \frac{1}{2}\int_{\mathcal{R}^d} |v|^2 f dv = \frac{1}{2}\rho|u|^2 + \frac{d}{2}\rho\theta. \tag{4}$$

The parameter $\nu > 0$ in (1) is the relaxation frequency which is defined as

$$\nu = \rho \tag{5}$$

other choices for the collision frequency can be considered such as $\nu = C\rho T^{1-\omega}$ with C a constant and ω which depends on the type of gas under consideration. For example, in the case of Argon it assumes the value $\omega = 0.81$ [19]. The parameter ε, instead, is the so-called Knudsen number and it is used to rescale the equation in time and space to ease the transition from the different time scales which characterize a kinetic model. The rescaling choice permits to study the different regimes easily. When the gas is dense and temperature is large, the relaxation frequency is typically very small. In this case, the gas appears macroscopically in equilibrium. In this situation, the flow can be described by a standard fluid model as the

compressible Euler system. This latter can be recovered in the limit $\varepsilon \to 0$ from (1) by observing that, in this case, the distribution function tends to the local Maxwellian M_f. The kinetic equation multiplied by $\left(1, v, \frac{1}{2}|v^2|\right)$ and integrated in velocity space reads then

$$\begin{aligned}
&\frac{\partial \rho}{\partial t} + \nabla_x \cdot (\rho u) = 0, \\
&\frac{\partial \rho u}{\partial t} + \nabla_x \cdot (\rho u \otimes u + pI) = 0, \\
&\frac{\partial E}{\partial t} + \nabla_x \cdot ((E+p)u) = 0, \\
&p = \rho\theta, \quad E = \frac{d}{2}\rho\theta + \frac{1}{2}\rho|u|^2,
\end{aligned} \tag{6}$$

i.e. it coincides with the compressible Euler equations, where p is the gas pressure. Using the Chapman-Enskog expansion higher order fluid models can be derived. In particular, the first order approximation of the distribution function $f = f_0 + \varepsilon f_1$ gives $f_0 = M_f$ and $f_1 = -(I - \Pi_M)v \cdot \nabla_x M_f$, with Π_M the orthogonal projection into the space spanned by the equilibrium M_f. This leads to the classical compressible Navier-Stokes equations

$$\partial_t \begin{pmatrix} \rho \\ \rho u \\ E \end{pmatrix} + \nabla_x \cdot \begin{pmatrix} \rho u \\ \rho u \otimes u + pI \\ (E+p)u \end{pmatrix} = -\varepsilon \begin{pmatrix} 0 \\ \nabla_x \cdot \sigma \\ \nabla_x \cdot (\sigma u + Q) \end{pmatrix}, \tag{7}$$

where $\sigma = -\mu(\nabla_x u + (\nabla_x u)^T - (2/d)\nabla_x \cdot uI)$ is the stress tensor and $Q = k\nabla_x T$ the heat flux.

Remark 1.

- When the velocity dimension is $d < 3$, model (1) naturally gives rise, in the macroscopic limit, to gas laws which differ from the standard one used for describing dense fluid flows. In particular, one gets $\gamma = \frac{2}{d} + 1$, with γ representing the ratio of the specific heats. Consequently, the one-dimensional case corresponds to $\gamma = 3$, the two-dimensional case to $\gamma = 2$ and the three-dimensional case to $\gamma = 5/3$. In order to overcome this problem and still avoiding three-dimensional discretizations in velocity, one can use the so-called Chu reduction [16]. The main idea, which this reduction relies on, is that under suitable velocity space symmetry assumptions, one can integrate the distribution function in the velocity phase space in one or two directions depending on the desired reduced dimension: respectively, the two- or the one-dimensional setting. This introduces an additional kinetic equation with a similar relaxation structure of the BGK one (1) and it permits to recover the correct equation of state obtained in the full three-dimensional case. Here, we do not make use of the Chu reduction and we postpone the use of such model and the relative issues to future investigations.
- Although the BGK model is able to describe the right hydrodynamic limit, it does not give rise to the correct Navier-Stokes asymptotic limit since the transport coefficients obtained by the Chapmann-Enskog expansion differ from those derived from the Boltzmann operator. An alternative consists in using a different relaxation model which allows the correct Prandtl number to be recovered, such as the ellipsoidal statistics BGK model [59]. We postpone the study of such a model to future investigations since this will need to study ad hoc time integration schemes.

2.1. Boundary conditions

The BGK equation needs the definition of suitable boundary conditions in space for $v \cdot n \geq 0$ and $x \in \partial\Omega$, where n denotes the unit normal, pointing inside the domain Ω. Usually, as for the case treated at the end of the paper, the boundary represents the surface of a solid object (the flow around a wing profile) and the particles of the gas that hit the surface interact with the atoms of the object and are reflected back into the domain Ω. Such boundary conditions are modeled by an expression of the form [18]

$$|v \cdot n| f(x, v, t) = \int_{v_* \cdot n < 0} |v_* \cdot n(x)| K(v_* \to v, x, t) f(x, v_*, t)\, dv_*, \tag{8}$$

where K is a given boundary kernel which permits to define the ingoing flux in terms of the outgoing flux. This boundary kernel is such that positivity and mass conservation at the boundaries are guaranteed. One common choice is represented by imposing for the ingoing velocities the following relation

$$f(x,v,t) = (1-\alpha)R_f(x,v,t) + \alpha M_f(x,v,t), \tag{9}$$

in which $x \in \partial\Omega$, $v \cdot n(x) \geq 0$. The coefficient α, with $0 \leq \alpha \leq 1$, is called the accommodation coefficient and one has

$$R_f(x,v,t) = f(x, v - 2n(n\cdot v), t), \quad M_f(x,v,t) = \mu(x,t) M_w(v). \tag{10}$$

Here, $M_w(v)$ is a Maxwellian distribution with unit mass, mean velocity corresponding to the speed of the object and fixed prescribed temperature, while the value of μ is determined by mass conservation at the wall, that is

$$\mu(x,t) \int\limits_{v\cdot n \geq 0} M_w(v)|v\cdot n| dv = \int\limits_{v\cdot n<0} f(x,v,t)|v\cdot n| dv. \tag{11}$$

In the numerical tests involving boundaries, we will consider specifically the case $\alpha = 1$ corresponding to full accommodation in which the re-emitted molecules have completely lost memory of the incoming molecules, except for conservation of the number of molecules. A second type of boundary conditions are the inflow boundary conditions where one assumes that the distribution function of the particles entering the domain is known, i.e.

$$f(x,v,t) = g(v,t), \quad x \in \partial\Omega, \quad v\cdot n > 0.$$

A typical example of such condition is used in shock wave calculations, where one assumes that the distribution function at the boundary of the computational domain is a Maxwellian $M_f(v)$ and that the incoming flux is distributed according to the Maxwellian flux $(v\cdot n)M_f(v)$, $v\cdot n > 0$. Finally, outflow boundaries are simply treated by upwinding, thus the distribution function is advected out of the computational domain.

3. The Discrete Velocity Models (DVM)

In a Discrete Velocity Model (DVM), one replaces the unbounded velocity space with a bounded set by truncation of the tails of the distribution function, which normally lives in a non compactly supported set. Successively, one discretizes this new space by means of a finite number of discrete points representing the discrete velocities that the particles can assume. This approach can be seen as a numerical technique but also as a new model for describing out of equilibrium gases [85]. In any way one wants to see it, the result is that one has to deal from the numerical point of view with N linear transport equations coupled through a suitable discretization of the interaction operator [85,78]. We now introduce the method and the notations, taking inspiration from [78]. We introduce a Cartesian grid $\mathcal{V}$

$$\mathcal{V} = \left\{ v_k = k\Delta v + a,\ k = k^{(i)},\ i = 1,..,d,\ a = (a_1,..,a_d) \right\}, \tag{12}$$

where a is an arbitrary vector, Δv is a constant mesh size in velocity and where the components of the index k have some given bounds $K^{(i)}$, $i = 1,..,d$. In this setting, the continuous distribution function f is replaced by the vector $f_{\mathcal{K}}(x,t)$ of size N. Each component of this vector is assumed to be an approximation of the distribution function f at location v_k:

$$f_{\mathcal{K}}(x,t) = (f_k(x,t))_k, \qquad f_k(x,t) \approx f(x,v_k,t). \tag{13}$$

Thus, the discrete ordinate kinetic model consists of the following system of equations to be solved

$$\partial_t f_k + v_k \cdot \nabla_x f_k = Q(f_k),\ k = 1,..,N, \tag{14}$$

which in the case of the BGK model can be directly made explicit

$$\partial_t f_k + v_k \cdot \nabla_x f_k = \frac{\nu}{\varepsilon}(\mathcal{E}_k[U] - f_k),\ k = 1,..,N, \tag{15}$$

i.e. $Q(f_k) = \frac{\nu}{\varepsilon}(\mathcal{E}_k[U] - f_k)$ with $\mathcal{E}_k[U]$ is a suitable approximation of M_f, e.g. $\mathcal{E}_k[U] = M_f(x,v_k,t)$, and $U = (\rho, \rho u, E)^T$ is the vector of the macroscopic quantities. Since the Maxwellian distribution depends on the distribution function f through its moments, it is necessary to recover them also in the discrete case. They are obtained thanks to discrete summations on the discrete velocity space:

$$U(x,t) = \sum_k \phi_k f_k(x,t)\,\Delta v = \langle \phi_k f_k(x,t)\rangle_{\mathcal{K}}, \tag{16}$$

with $\phi_k = (1, v_k, \frac{1}{2}|v_k|^2)$ representing the discrete collision invariants.

Remark 2.

- The number N of discrete velocity is chosen as a compromise between precision and computational cost. If N is set too small then the flow cannot be described correctly: in general not all states can be reached in terms of temperature and mean velocity by a discrete ordinate method.
- A way to represent better the physical solution would be to change the support of the distribution function and the nodes where it is defined as a function of the solution itself [5,53,54]. Here, we do not discuss this possibility and we postpone this study to future work.
- The exact conservation of macroscopic quantities is impossible, because in general the support of the distribution function is non compact. This is the case for instance of the Maxwellian equilibrium distribution M_f as well as the case of the Boltzmann collision integral defined on the entire space $\mathcal{R}^d$. Thus, in order to conserve macroscopic variables, different strategies can be adopted, two of them are described in [56,78].
- In this work, we take the number of discrete points sufficiently large and we perform a truncation of the space such that the loss of conservation is negligible. However, we stress that all the schemes detailed in what follows can be adapted to the case in which perfect conservation is required [16].

4. Space discretization

We discuss now the space discretization of the system of equations (14), i.e. the space discretization of the discrete ordinate model. This is done via a particular WENO reconstruction. In particular, we discuss here how, given the set of cell averages corresponding to the distribution function values f_k^n, one obtains a high order polynomial reconstruction representing the solution in the entire space. The same reconstruction for which we give details in the sole case of the distribution function, will be used next for obtaining high order approximations of the fluxes and of the source term represented by the collisional operator $Q(f)$ in the finite volume framework. The basic idea of WENO reconstructions is the following: get high order polynomial through convex combinations of the point values of lower degree polynomials employing smaller stencils. The coefficients of the convex combination have some optimal linear values that are determined by satisfying accuracy requirements. Then, the real coefficients employed in the reconstruction are derived from the optimal values by a nonlinear procedure which permits to avoid oscillatory solutions, according to Godunov's theorem [57]. The CWENO procedure is based on the same idea of producing an high-order cell centered non oscillating polynomials. It differs from WENO by the fact that the linear weights do not need to satisfy any accuracy requirements. Consequently, these values can be chosen independently from the mesh topology and also independently from the location of the points where the polynomials should be evaluated. Moreover, CWENO employs one single set of linear weights and thus one single set of nonlinear weights that are valid for any point in the cell. Thus, CWENO provides an entire reconstruction polynomial that is defined everywhere inside a cell. CWENO methods are relatively new techniques, examples of multi-dimensional finite volume CWENO schemes have been presented in [73,74,45] for Cartesian meshes and in [87] on two-dimensional quadrangular meshes. A comparison of different CWENO techniques has been recently forwarded in [22]. Up to our knowledge, CWENO reconstruction operators have never been applied to kinetic equations before. We give now the details about how the grid, which is used for the polynomial reconstruction, is realized.

4.1. Construction of the polygonal mesh

From now on, we consider two-dimensional arbitrarily shaped domains Ω and we detail the CWENO method on these domains. In order to discretize them, we employ a centroid based Voronoi-type tessellation made of N_p non overlapping polygons $P_i, i = 1, \dots N_p$. The idea is to represent the unknowns and in particular the distribution function $f(x, v, t)$ via high order polynomials in each Voronoi polygon. The grid is constructed by setting the position of N_p points, called generator points, uniformly inside Ω as well as on its boundary. Their coordinates are denoted as $x_{c_i}, i = 1, \dots, N_p$. Next, a Delaunay triangulation having these generators x_{c_i} as vertexes of the triangles is realized. In this triangulation, the circumcircle of each triangle is not allowed to contain any other generator point. One can prove that, under this condition, the triangulation for every points is uniquely defined, except for circles containing more than three generator points. In this situation, the Delaunay triangulation may contain degenerate cases. A solution is presented in [15], which permits to give back uniqueness of the triangulation and it is employed here.

Once the *primal* triangulation is realized, then each generator point x_{c_i} is associated to a centroid based Voronoi element P_i by connecting counterclockwise the centers of mass of all the Delaunay triangles having this generator point as a vertex. Now, given a Voronoi polygon P_i we denote by

$$\mathcal{V}(P_i) = \{v_{i_1}, \dots, v_{i_j}, \dots, v_{i_{N_{V_i}}}\}, \tag{17}$$

the set of its N_{V_i} Voronoi neighbors, by

$$\mathcal{E}(P_i) = \{e_{i_1}, \dots, e_{i_j}, \dots, e_{i_{N_{V_i}}}\}, \tag{18}$$

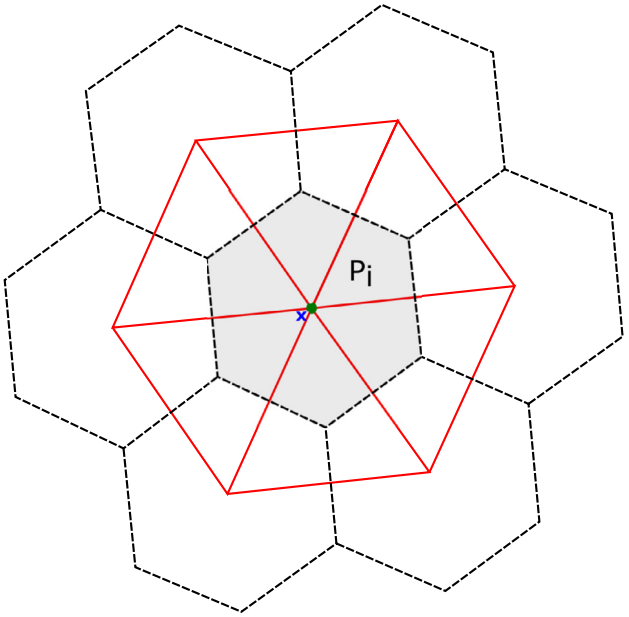

Fig. 1. Example of the construction of the Voronoi tessellation (black dotted line) starting from the Delaunay triangulation (red solid line). The generator point $x_{c,i}$ for polygon P_i is marked with a blue cross, while the barycenter x_{b_i} of the Voronoi control volume is represented by a green circle. To each generator point corresponds a Voronoi polygon. (For interpretation of the colors in the figure(s), the reader is referred to the web version of this article.)

the set of its N_{V_i} edges, and by

$$\mathcal{D}(P_i) = \{d_{i_1}, \dots, d_{i_j}, \dots, d_{i_{N_{V_i}}}\}, \tag{19}$$

the set of its N_{V_i} vertexes ordered in a counter clock manner. Finally, the barycenter of a Voronoi polygon P_i is computed and denoted by x_{b_i}: with the center of mass defined as

$$x_{b_i} = \frac{1}{|P_i|} \int_{P_i} x\, dx. \tag{20}$$

Note that usually this does not coincide with the generator point (see Fig. 1 for a visual explanation).

Once the grid is set, we connect the barycenters x_{b_i} with each vertex of $\mathcal{D}(P_i)$ and we subdivide the Voronoi polygon P_i in N_{V_i} triangles denoted as

$$\mathcal{T}(P_i) = \{T_{i_1}, \dots, T_{i_j}, \dots, T_{i_{N_{V_i}}}\}. \tag{21}$$

This sub-triangulation is in practice used to numerically integrate all needed data over the polygon. The above procedure completely defines the mesh, as the one shown in Fig. 2 for instance. Notice that the sub-triangulation used in our framework allows each polygonal mesh to be split and properly employed for the discretization of the computational domain Ω. As such, even a simplex triangular mesh can be seen as a polygonal grid, in which each polygon is split into three sub-triangles. In the next paragraph, we employ this space mesh to describe the polynomial reconstruction.

4.2. Polynomial CWENO reconstruction

We discuss now the data interpolation. In this work we rely on a CWENO reconstruction strategy that can be designed along the lines introduced in [23]. Specifically, the WENO reconstruction algorithm makes use of the *polynomial* formulation [47], thus we do not adopt the original *pointwise* WENO scheme [67,60,96]. This approach allows more flexibility regarding the choice of the linear weights and it easily applies to general unstructured meshes in multiple space dimensions [45,55] while achieving the formal order of accuracy.

The continuous distribution function $f(x, v, t)$ has been replaced by the vector $f_{\mathcal{K}}(x, t)$ in the previous Section. In this setting, the cell averages of each component of the vector representing the distribution function at time t^n are obtained by

$$\bar{f}^n_{k,i} = \frac{1}{|P_i|} \int_{P_i} f_k(x, t^n) dx, \ \forall k \in \mathcal{K}, \ x \in P_i, \ i \in [1, N_p], \tag{22}$$

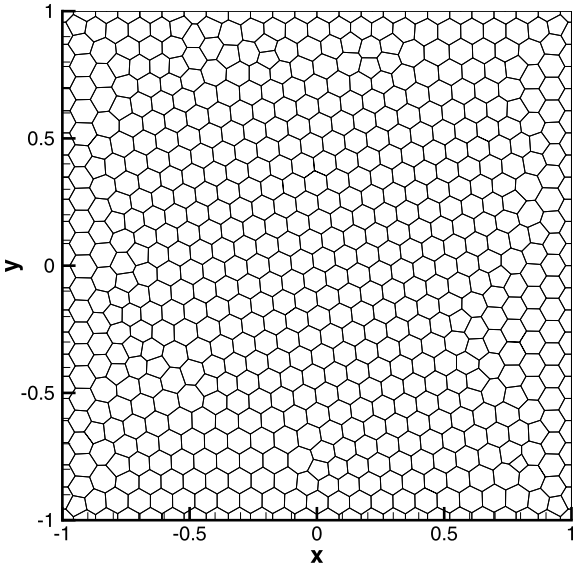

Fig. 2. Example of an arbitrarily polygonal unstructured mesh obtained from the description in Section 4.1.

with $|P_i|$ representing the volume of cell P_i. In what follows, $w_{k,i}(x,t^n)$ will be the high order non-oscillatory polynomial representation of the distribution function $f(x,v,t)$ in its discrete velocity sense, for each cell $P_i,\ i=1,..,N_p$. The reconstruction can be summarized by the following three steps: definition of a high order *optimal* polynomial function, definition of a set of *low order* polynomials, nonlinear combination between the high order and the low order functions to get the highest accurate possible non oscillating reconstruction operators. In the description outlined hereafter, we leave freedom to the *optimal* polynomial to assume an arbitrary degree M. This provides a theoretical spatial accuracy of order $(M+1)$. The number of degrees of freedom (*dof*) associated to such reconstruction depends clearly on the spatial dimension d. Here, we fix $d=2$ consistently with the previous Section. Correspondingly, the number of unknowns $\mathcal{M}$, or degrees of freedom, is given by

$$\mathcal{M}(M,d)=\frac{1}{d!}\prod_{l=1}^{d}(M+l)=\frac{1}{2}(M+1)(M+2)=\mathcal{M}(M,2)=\mathcal{M}(M). \tag{23}$$

We proceed now in order to uniquely define the *dof* starting from the known cell averages values $\bar{f}^n_{k,i}$ of the distribution function at time t^n. First, we compute the polynomial p_{opt} of degree M. Following [72,87], we consider a central stencil $\tilde{\mathcal{S}}_i$ composed of $n_e=d\cdot\mathcal{M}(M)$ cells

$$\tilde{\mathcal{S}}_i=\bigcup_{l=1}^{n_e}P_{j(l)}, \tag{24}$$

where $j=j(l)$ denotes a mapping from the set of integers $l\in[1,n_e]$ to the global indexes j used to sort the cells in the mesh. The stencil $\tilde{\mathcal{S}}_i$ is composed by the cell P_i where the solution needs to be computed and by its neighbors, added isotropically in space until the needed n_e number of elements is reached (see Fig. 3). For convenience, we assume that $j(1)=i$ so that the first cell in the stencil is always the element for which we are computing the reconstruction. As suggested in [6], on general unstructured grids, the total number of stencil elements n_e must be *larger* than the number of degrees of freedom $\mathcal{M}(M)$ needed to reach the formal order of accuracy, hence a safety factor of $d=2$ is considered. This is necessary to avoid ill-conditioning of the resulting reconstruction matrices. The polynomial $p_{opt,i}$ relative to the stencil $\tilde{\mathcal{S}}_i$, is then defined by imposing that its cell average on each polygonal element P_j matches the average of the distribution function $\bar{f}^n_{k,j}$ in a *weak sense*. This means that we impose the polynomial function to match exactly the value of the distribution function in the element P_i. Simultaneously, we ask for this function to minimize the L^2 distance from values assumed by the distribution in the remaining elements of the stencil $\tilde{\mathcal{S}}_i$. In fact, since $n_e>\mathcal{M}$ by definition, an overdetermined linear system is clearly obtained. As a consequence, it is not possible to exactly match the average values assumed by the distribution function in the cells as a result of the time evolution of the solution. Thus, a constrained least-squares approach, as the one proposed in [47], is used to define this function uniquely. This reads

$$p_{opt,i} = \underset{p\in\mathcal{P}_i}{\operatorname{argmin}} \sum_{P_j\in\tilde{\mathcal{S}}_i} \left(\bar{f}^n_{k,j} - \frac{1}{|P_j|}\int_{P_j} p(x)dx \right)^2 , \tag{25}$$

where $\mathcal{P}_i$ is the set of all polynomials $\mathbb{P}_M$ of degree at most M, satisfying

$$\mathcal{P}_i = \left\{ p\in\mathbb{P}_M : \bar{f}^n_{k,i} = \frac{1}{|P_i|}\int_{P_i} p(x)dx \right\} \subset \mathbb{P}_M. \tag{26}$$

In other words, the function $p_{opt,i}$ is, among all the possible polynomials of degree M, the only one that shares the same cell average of the distribution function in the cell P_i, i.e. $\bar{f}^n_{k,i}$, while being close in the least-square sense to the other cell averages in the stencil $\tilde{\mathcal{S}}_i$. The polynomial $p_{opt,i}$, obtained from the above minimization step, is then practically expressed through the following *conservative* expansion

$$p_{opt,i}(x,t^n) = \sum_{\ell=1}^{\mathcal{M}} \varphi_\ell(x)\hat{p}^n_{l,i}, \tag{27}$$

where $\hat{p}^n_{l,i}$ denote the unknown expansion coefficients of each reconstruction which employs the stencil $\tilde{\mathcal{S}}_i$. The basis functions φ_ℓ are defined using a Taylor series in the space variables x of components (x_1, x_2) of degree M. This expansion is directly defined on the physical element P_i, expanded about its center of mass x_{b_i} and normalized by the characteristic length h_i of the element (the radius of the circumcircle of P_i)

$$\varphi_\ell(x_1,x_2)|_{P_i} = \frac{(x_1-x_{b_i,1})^p}{h_i^p}\,\frac{(x_2-x_{b_i,2})^q}{h_i^q} - \int_{P_i} \frac{(x_1-x_{b_i,1})^p}{h_i^p}\,\frac{(x_2-x_{b_i,2})^q}{h_i^q}\,dx, \tag{28}$$

$$\ell = 0,\dots,\mathcal{M}, \quad (p,q) = 0,\dots,M,\ p+q\le M.$$

In the above construction, the integrals appearing in (25)-(28) are computed in each Voronoi polygon P_i by summing the contribution of each sub-triangle $T\in\mathcal{T}(P_i)$. This type of numerical integration obtained by decomposition of the polygonal surface into sub-elements is repeated each time a space integral appears in the rest of the article. On each sub-triangle, finally, we employ $(M+1)^2$ Gauss quadrature points defined by the conical product of the one-dimensional formulae [89].

In order to complete the CWENO reconstruction, one needs now a series of low degree polynomials with the scope of stabilizing the high degree reconstruction performed above. These are obtained starting from the Voronoi polygon P_i and by selecting a series of subsets of the N_{V_i} Voronoi neighbors $\mathcal{V}(P_i)$ to build up a new series of stencils. Thanks to these subsets, one then constructs exactly N_{V_i} interpolating polynomials of degree $M^L = 1$. The stencils of these polynomials, S^L_i with $L\in[1, N^n_{V_i}]$, contain exactly $\hat{n}_e = \mathcal{M}(M^L) = 3$ cells. Each S^L_i always includes the central cell P_i and two consecutive neighbors belonging to $\mathcal{V}(P_i)$. The reconstruction stencils are indeed obtained as follows: the central stencil is filled starting with the element under consideration, then its Neumann neighbors are considered and finally other elements are recursively added as neighbors of these neighbors, until the desired total number of objects n_e in the stencil is reached. The one-sided stencils are always composed by three elements in 2D, namely the element itself P_i, one direct neighbor P_j and the other Neumann neighbor that is a direct neighbor of both P_i and P_j. An example of stencils $\tilde{\mathcal{S}}_i$ and S^L_i for a polygon with $N^n_{V_i} = 6$ and $M = 2$ is reported in Fig. 3.

For each stencil S^L_i, the linear polynomial p^L_i is obtained through the unique solution of the system

$$p^L_i\in\mathbb{P}_1 \text{ s.t. } \forall P_l\in S^L_i : \bar{f}^n_{k,l} = \frac{1}{|P_l|}\int_{P_l} p^L_i(x)\,dx, \tag{29}$$

where l indicates the mesh element belonging to the stencil S^L_i. It remains to define the central polynomial p^0_i. This is defined by difference between the polynomial $p_{opt,i}$ and the linear combination of the polynomial functions p^L_i of lower degree [23], that is

$$p^0_i = \frac{1}{\lambda_0}\left(p_{opt,i} - \sum_{L=1}^{N_{V_i}} \lambda_{L,i}\,p^L_i \right) \in \mathbb{P}_M, \tag{30}$$

where $\lambda_{0,i},\dots,\lambda_{N_{V_i}}$ are positive coefficients such that

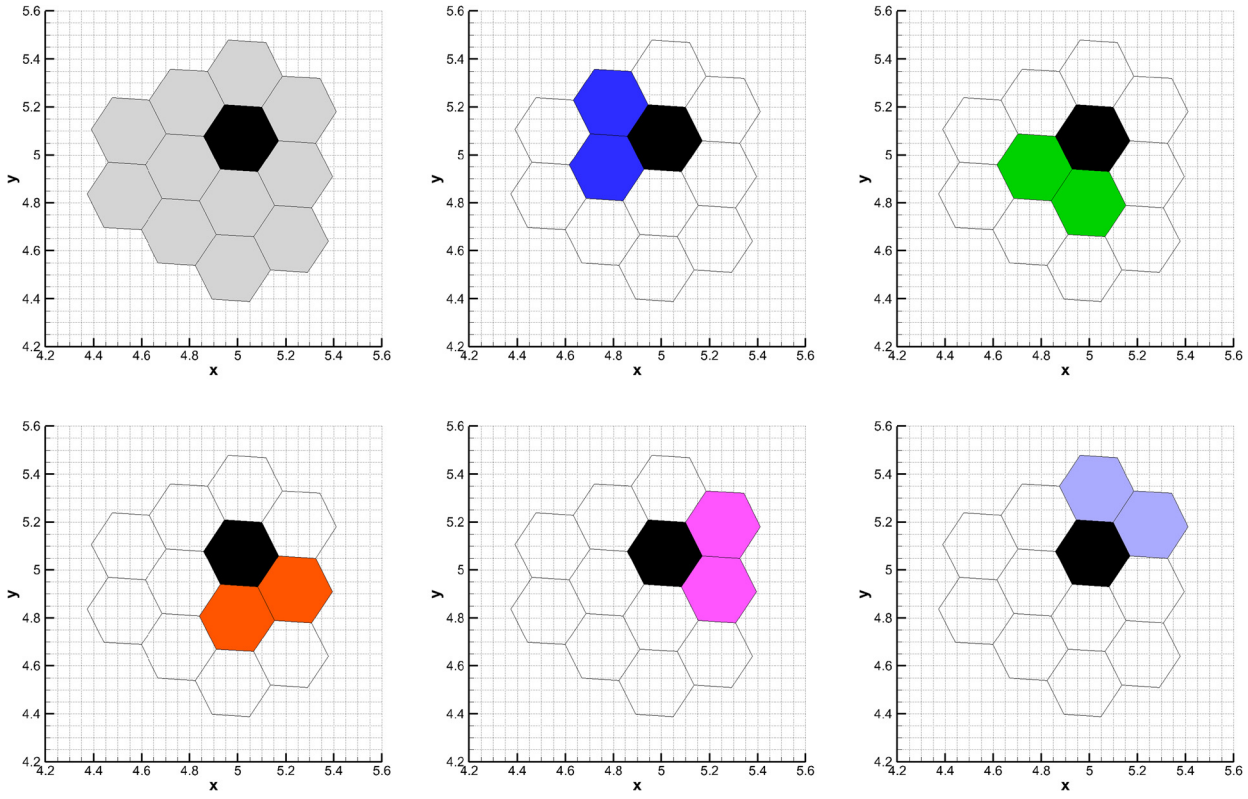

Fig. 3. Reconstruction stencils for second order degree optimal polynomials, i.e. $M = 2$. The total number of neighbors is $n_e = 12$. The central P_2 stencil is highlighted in gray, while five (out of six) one-sided P_1 reconstruction stencils are shown with different colors.

$$\sum_{s=0}^{N_{V_i}} \lambda_{s,i} = 1 := \lambda_{sum}. \tag{31}$$

This is enough to assure conservation. The central polynomial p_i^0 defined by (30) guarantees that the linear combination of the polynomials $p_i^0, \dots, p_i^{N_{V_i}}$ with the coefficients $\lambda_0, \dots, \lambda_{N_{V_i}}$ is equal to $p_{opt,i}$. This is the reason why these coefficients are typically called *optimal coefficients* and the accuracy of the CWENO reconstruction does *not* depend on the choice of the optimal coefficients. The linear weights are a normalization which sums up to unity, starting from the values $\lambda_{0,i} = C/\lambda_{sum}$ for $\mathcal{S}_i^0$ with $C \gg 1$ and $\lambda_{L,i} = 1/\lambda_{sum}$ for all other polynomials. Here we set $C = 200$ and $\lambda_{s,i} = 1$. A last step consists in the standard WENO nonlinear combination of the polynomials p_i^L with p_i^0. Thus, the final polynomial $f_{i,k}(x, t^n)$ is defined by this hybridization among all stencils $s \in [0, N_{V_i}]$

$$f_{i,k}(x, t^n) = \sum_{s=0}^{N_{V_i}} \omega_s p_i^s(x), \tag{32}$$

where the nonlinear weights ω_s are given by the standard expressions

$$\omega_s = \frac{\tilde{\omega}_s}{\sum_{s=0}^{N_{V_i}} \tilde{\omega}_s}, \qquad \text{with} \qquad \tilde{\omega}_s = \frac{\lambda_s}{(\sigma_s + \epsilon)^r}, \tag{33}$$

where $\epsilon = 10^{-14}$ and $r = 4$ are chosen according to [47], and the oscillation indicators are given by

$$\sigma_s = \sum_l \left(\hat{p}_{l,i}^s\right)^2, \tag{34}$$

with $\hat{p}_{l,i}^s$ representing the expansion coefficients (27) the polynomial defined on stencil s. As an effect of the nonlinear combination, one gets that in smooth areas, $\omega_s \simeq \lambda_s$ and then $w_{k,i} \simeq p_{opt,i}$, which means that optimal accuracy is recovered. On the other hand, close to a discontinuity, p_i^0 is expected to have oscillatory behaviors, leading to $\omega_s \simeq 0$. This gives a low order non-oscillatory distribution function reconstruction employed to define the finite volume method.

4.3. Finite volume approach

We discuss now the finite volume method approach. In particular, thanks to the CWENO reconstruction discussed above and employing the unstructured grid detailed in Section 4.1, we introduce a high order in space finite volume scheme. In Section 5, we explain how high order in time discretization is achieved. We start by integrating equation (14) on each control volume P_i obtaining

$$\partial_t \int_{P_i} f_k \, dx + \int_{P_i} v_k \cdot \nabla_x f_k \, dx = \int_{P_i} Q(f_k) \, dx, \; k = 1, .., N, \; i = 1, .., N_p, \tag{35}$$

where $Q(f_k)$ represents a high order space reconstruction in the control volume P_i of the collision BGK operator

$$Q(f_k) = \frac{\nu}{\varepsilon}(\mathcal{E}_k[U] - f_k)$$

Now, using the divergence theorem, we get

$$\partial_t \int_{P_i} f_k \, dx = -\int_{\partial P_i} L(f_k) \cdot \, n_i \, dS + \int_{P_i} Q(f_k) \, dx, \quad k = 1, .., N, \; i = 1, .., N_p, \tag{36}$$

where we have denoted by n_i the unit outward normal to the element P_i and by $L(f_k)$ the flux function $(v_k f_k)$. The surface integral can be decomposed over the faces of ∂P_i of the element P_i. This gives

$$\partial_t \int_{P_i} f_k \, dx = -\sum_{j=1}^{N_{V_i}} \int_{\partial P_{i_j}} L(f_k) \cdot \, n_{ij} \, dS + \int_{P_i} Q(f_k) \, dx, \quad k = 1, .., N, \; i = 1, .., N_p, \tag{37}$$

with ∂P_{i_j} denoting the face shared between element P_i and its neighbor P_j. Finally, by introducing a first order in time explicit Euler discretization, we get

$$\int_{P_i} f_k^{n+1} \, dx = \int_{P_i} f_k^n \, dx - \Delta t \sum_{j=1}^{N_{V_i}} \int_{\partial P_{i_j}} L(f_k^n) \cdot \, n_{ij} \, dS + \Delta t \int_{P_i} Q(f_k^n) \, dx, \quad k = 1, .., N, \; i = 1, .., N_p, \tag{38}$$

which is equivalent, using the finite volume interpretation, to

$$\bar{f}_{k,i}^{n+1} = \bar{f}_{k,i}^n - \frac{\Delta t}{|P_i|} \sum_{j=1}^{N_{V_i}} \int_{\partial P_{i_j}} L(f_k^n) \cdot \, n_{ij} \, dS + \frac{\Delta t}{|P_i|} \int_{P_i} Q(f_k^n) \, dx, \qquad k = 1, .., N, \quad i = 1, .., N_p. \tag{39}$$

Now, in order to obtain a high order in space scheme, we employ the CWENO reconstruction presented in the previous paragraph. Thus, the distribution function f_k^n at time t^n in Eqn. (38) is replaced by the high order polynomial function, namely $f_{k,i}^n = f_{i,k}(x, t^n)$ in each element P_i according to (32). This gives the cell average values for every discrete velocity at time t^{n+1}

$$\bar{f}_{k,i}^{n+1} = \frac{1}{|P_i|} \int_{P_i} f_{k,i}^{n+1} \, dx, \tag{40}$$

used for the next CWENO reconstruction at the next time level.

It remains to detail the boundary fluxes which permits to share the information between the neighbors. These are obtained by the Rusanov flux [86] which reads

$$L(f_{k,i}^n) \cdot \, n = \mathcal{L}(f_{k,i}^{n,-}, f_{k,i}^{n,+}) \cdot n, \tag{41}$$

where $(f_{k,i}^{n,-})$ is the inner and $(f_{k,i}^{n,+})$ is the outer high order boundary extrapolated values and

$$\mathcal{L}(f_{k,i}^{n,-}, f_{k,i}^{n,+}) \cdot n = \frac{1}{2}\left(L(f_{k,i}^{n,+}) + L(f_{k,i}^{n,-})\right) \cdot n_{ij} - \frac{1}{2} s_{\max}\left(f_{k,i}^{n,+} - {}_{k,i}^{n,-}\right), \tag{42}$$

with $s_{\max}$ denoting the maximum eigenvalue of the system corresponding to $\max_{\mathcal{K}}(|v_k|)$ and n_{ij} representing the unit outward pointing normal vector to the cell boundary. The above scheme, apart from being only first order in time, suffers from the stiffness of the equation when the Knudsen number is small. Next, wed discuss high order time discretizations and a remedy to the stiffness of the kinetic equations.

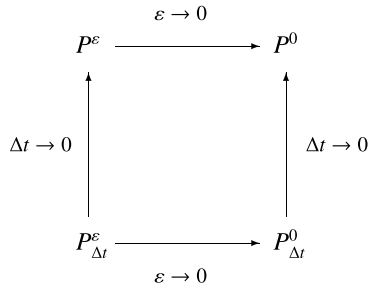

Fig. 4. P^ε is the original singular perturbation problem (kinetic model) and $P^\varepsilon_{\Delta t}$ its numerical approximation characterized by a discretization parameter Δt. The *asymptotic-preserving (AP) property* corresponds to the request that $P^\varepsilon_{\Delta t}$ is a consistent discretization of P^0 (the compressible Euler equations) as $\varepsilon \to 0$ independently of Δt.

5. Time discretization

We discuss, in this part, how to improve the time discretization. This is done, as anticipated in the Introduction, through the use of a particular class of Runge-Kutta schemes called Implicit-Explicit (IMEX) Runge-Kutta methods [3,83,42]. We recall that one of the major difficulties in solving kinetic equations is related to the capability of handling the different space and time scales characterizing the physical model. In particular, for the problems we are interested in, situations close to the so-called fluid regimes arise frequently. In these cases, the mean free path between two collisions is very small, thus it translates in a small value of the scaling parameter ε. From the numerical point of view, this implies that the problem becomes stiff. In the limit $\varepsilon \to 0$, we formally obtain that the kinetic equation is equivalent to the compressible Euler macroscopic fluid equations. For small but non zero values of the Knudsen number, the evolution equation for the moments can be derived and it originates the compressible Navier-Stokes equations (see Section 2).

Our aim is precisely to work with schemes that are capable of capturing the fluid-limit without time step limitations due to the fast scale dynamic. This request is equivalent to the notion of *asymptotic-preserving (AP)* schemes [43,30,31,69,46,13]. A frequently adopted formal definition for such schemes [68,83,42] in the context of kinetic equations close to the fluid limit that we recall here says that: a consistent time discretization method of a given step size Δt is *AP* if, independently of Δt, in the limit $\varepsilon \to 0$ becomes a consistent time discretization method for the compressible Euler equations. If, in addition, the scheme preserves the order of accuracy in time in the stiff limit, we say that the scheme is *asymptotically accurate (AA)*. Fig. 4 depicts the standard diagram which AP methods obey to. We introduce now the general formulation of an IMEX scheme for the kinetic equations. To this aim, we use the finite volume formulation (39) of our method which we recall here for clarity

$$\bar{f}^{n+1}_{k,i} = \bar{f}^{n}_{k,i} - \frac{\Delta t}{|P_i|} \sum_{j=1}^{N_{V_i}} \int_{\partial P_{i_j}} L(f^n_{k,i}) \cdot n_{ij}\, dS + \frac{\Delta t}{|P_i|} \int_{P_i} Q(f^n_{k,i})\, dx, \qquad k = 1,..,N, \quad i = 1,..,N_p, \tag{43}$$

where the high order CWENO reconstruction $f^n_{k,i}$ substitutes the continuous in space functions f^n_k in the fluxes and source term. The general IMEX setting reads

$$\bar{F}^{(l)}_{k,i} = \bar{f}^{n}_{k,i} - \Delta t \sum_{m=1}^{l-1} \tilde{a}_{lm} \langle L(F^{(m)}_{k,i}) \rangle_x + \Delta t \sum_{m=1}^{\iota} a_{lm} \langle Q(F^{(m)}_{k,i}) \rangle_x \tag{44}$$

$$\bar{f}^{n+1}_{k,i} = \bar{f}^{n}_{k,i} - \Delta t \sum_{m=1}^{\nu} \tilde{w}_m \langle L(F^{(m)}_{k,i}) \rangle_x + \Delta t \sum_{m=1}^{\iota} w_m \langle Q(F^{(m)}_{k,i}) \rangle_x, \tag{45}$$

where $\bar{F}^{(l)}_{k,i}$ are the so-called stage values of the Runge-Kutta method which identify the cell averages of the solution at different time levels between $[t^n, t^{n+1}]$. Correspondingly, the quantities $F^{(l)}_{k,i}$ are their high order reconstruction counterparts. Using these values it is possible to determine the quantity

$$\langle L(F^{(l)}_{k,i}) \rangle_x = \frac{1}{|P_i|} \sum_{j=1}^{N_{V_i}} \int_{\partial P_{i_j}} L(F^{(l)}_{k,p}) \cdot n_{ij}. \tag{46}$$

Moreover, we have that

$$\langle Q(F^{(l)}_{k,i}) \rangle_x = \frac{1}{|P_i|} \int_{P_i} Q(F^{(l)}_{k,i})\, dx, \tag{47}$$

where the integral is obtained by a suitable Gauss formula in which for every discrete velocity k the cell average is substituted with its high order polynomial reconstruction in the cell P_i. From (47), it is clear that the direct application of such method is very difficult in practice. This, in fact, would need the inversion of a nonlinear system involving the operator $\langle Q(F_{k,i}^{(l)})\rangle_x$ at each stage of the Runge-Kutta time stepping. We will come back to this question later to find a remedy to this situation. Let before introduce the matrices $\tilde{A} = (\tilde{a}_{lm})$, $\tilde{a}_{lm} = 0$ for $m \geq l$ and $A = (a_{lm})$. They are $\iota \times \iota$ matrices such that the resulting scheme is explicit in $L(f_k)$, and implicit in $Q(f_k)$. An IMEX Runge-Kutta scheme is characterized by these two matrices and by the coefficient vectors $\tilde{w} = (\tilde{w}_1, .., \tilde{w}_\iota)^T$, $w = (w_1, .., w_\iota)^T$. The type of implicit schemes we consider are all such that $a_{lm} = 0$, for $m > l$: this permits to assure that the transport term is always evaluated explicitly and it is of crucial importance for reducing the computational effort. We refer to them as to DIRK implicit methods. Classically, the schemes can be efficiently resumed by a double Butcher tableau

$$\begin{array}{c|c} \tilde{c} & \tilde{A} \\ \hline & \tilde{w}^T \end{array} \qquad \begin{array}{c|c} c & A \\ \hline & w^T \end{array}$$

where the coefficients $\tilde{c}$ and c are given by the classical relation $\tilde{c}_l = \sum_{m=1}^{l-1} \tilde{a}_{lm}$, $c_l = \sum_{m=1}^{l} a_{lm}$. We refer to [3,83] for more details on the order conditions for such methods. As previously stated, the proposed IMEX schemes require the inversion of the collision operator, which cannot be done directly due to the nonlinear polynomial reconstruction needed in the finite volume setting. To that aim, we observe that this high order integration can be conveniently written as

$$\langle Q(F_{k,i}^{(l)})\rangle_x = \frac{1}{|P_i|}\int_{P_i} Q(F_{k,i}^{(l)})\,dx = Q(\bar{F}_{k,i}^{(l)}) + O(\Delta x^2), \tag{48}$$

where Δx is the typical mesh size and $\bar{F}_{k,i}^{(l)}$ are the cell average quantities at the stage l. Then the time integrator can be recast as

$$\bar{F}_{k,i}^{(l)} = \bar{f}_{k,i}^{n} - \Delta t \sum_{m=1}^{l-1} \tilde{a}_{lm} \left(\langle L(F_{k,i}^{(m)})\rangle_x + \Delta Q(F_{k,i}^{(m)}) \right) + \Delta t \sum_{m=1}^{l} a_{lm} Q(\bar{F}_{k,i}^{(m)}) \tag{49}$$

$$\bar{f}_{k,i}^{n+1} = \bar{f}_{k,i}^{n} - \Delta t \sum_{m=1}^{\nu} \tilde{w}_m \left\langle L(F_{k,i}^{(m)})\rangle_x + \Delta Q(F_{k,i}^{(m)}) \right) + \Delta t \sum_{m=1}^{\iota} w_m \bar{Q}(\bar{F}_{k,i}^{(m)}), \tag{50}$$

where the quantities $\Delta Q(F_{k,i}^{(m)})$ are given by

$$\Delta Q(F_{k,i}^{(m)}) = \langle Q(F_{k,i}^{(m)})\rangle_x - Q(\bar{F}_{k,i}^{(m)}), \tag{51}$$

i.e. they represent the difference between the high order evaluation of the source term and its cell average and are taken explicit in the IMEX formulation. This permits a direct evaluation of the implicit terms without resorting to the approximate solution of nonlinear systems despite the nonlinearity of the function which defines the equilibrium state $M_f(x, v, t)$. To better understand this, let us remark that the stage evaluation of the cell average of the distribution function (49) can be rewritten as

$$\bar{F}_{k,i}^{(l)} = \bar{f}_{k,i}^{n} - \Delta t \sum_{m=1}^{l-1} \tilde{a}_{lm} \left(\langle L(F_{k,i}^{(m)})\rangle_x + \Delta Q(F_{k,i}^{(m)}) \right) + \Delta t \sum_{m=1}^{l} a_{lm} Q(\bar{F}_{k,i}^{(m)}) + \Delta t \int_{P_i} \frac{\nu}{\varepsilon} (\mathcal{E}_k[\bar{U}_i^{(l)}] - \bar{F}_{k,i}^{(l)})\,dx, \tag{52}$$

where the only implicit term is the diagonal factor $\frac{\nu}{\varepsilon}(\mathcal{E}_k[\bar{U}_i^{(l)}] - \bar{F}_{k,i}^{(l)})$ in which $\mathcal{E}_k[\bar{U}_i^{(l)}]$ depends only on the first three moments of the distribution function $\bar{U}_i^{(l)}$. These are easily obtained by integrating in velocity space the cell centered values of the distribution function

$$\bar{U}_i^{(l)} = \sum_k \phi_k \bar{F}_{k,i}^{(l)} \Delta v = \langle \phi \bar{F}_i^{(l)} \rangle_{\mathcal{K}}. \tag{53}$$

Once these values are given and the cell centered values of the Maxwellian distribution are computed, then the integrals in (52) can all be directly evaluated in the case of the cell average values and by using a suitable Gauss integration formula in the case in which the CWENO polynomials have to be integrated. Finally, (52) can also be directly computed by moving on the left hand side the sole term which remains implicit: $\bar{F}_{k,i}^{(l)}$. To have a completely determined method, it remains to explain

how the moments $\bar{U}_i^{(l)}$ are obtained. This is done by integrating equation (52) against the discrete collision invariants ϕ_k in velocity space which gives

$$\langle \phi \bar{F}_i^{(l)} \rangle_{\mathcal{K}} = \langle \phi \bar{f}_i^n \rangle_{\mathcal{K}} - \Delta t \sum_{m=1}^{l-1} \tilde{a}_{lm} \langle \phi \langle L(F_{k,i}^{(m)}) \rangle_x \rangle_{\mathcal{K}}. \tag{54}$$

As a consequence, $\bar{U}_i^{(l)}$ and thus $\mathcal{E}_k[\bar{U}_i^{(l)}]$ can be explicitly evaluated and then the scheme (49)-(50) is *explicitly* solvable. This concludes the presentation of the scheme. The next part is devoted to some analysis of the new methods proposed.

5.1. Properties of the IMEX schemes

We want now to derive conditions for these new IMEX schemes to be AP and asymptotically accurate. Some preliminary definitions are necessary, see [42] for details.

Definition 1. We call an IMEX-RK method of *type A* if the matrix $A \in \mathbb{R}^{\iota \times \iota}$ is invertible, or equivalently $a_{ii} \neq 0$, $i = 1, \dots, \iota$. We call an IMEX-RK method of *type CK* if the matrix A can be written as

$$A = \begin{pmatrix} 0 & 0 \\ a & \hat{A} \end{pmatrix}, \tag{55}$$

with $a = (a_{21}, \dots, a_{\iota 1})^T \in \mathbb{R}^{(\iota-1)}$ and the submatrix $\hat{A} \in \mathbb{R}^{(\iota-1) \times (\iota-1)}$ invertible, or equivalently $a_{ii} \neq 0$, $i = 2, \dots, \iota$. In the special case $a = 0$, $w_1 = 0$ the scheme is said to be of *type ARS* and the DIRK method is reducible to a method using $\iota - 1$ stages.

We will also make use of the following representation of the matrix $\tilde{A}$ in the explicit Runge-Kutta method

$$\tilde{A} = \begin{pmatrix} 0 & 0 \\ \tilde{a} & \hat{\tilde{A}} \end{pmatrix}, \tag{56}$$

where $\tilde{a} = (\tilde{a}_{21}, \dots, \tilde{a}_{\iota 1})^T \in \mathcal{R}^{\iota-1}$ and $\hat{\tilde{A}} \in \mathcal{R}^{\iota-1 \times \iota-1}$.

Definition 2. The IMEX-RK method is said to be *globally stiffly accurate (GSA)* if

$$a_{\nu i} = w_i, \quad \tilde{a}_{\nu i} = \tilde{w}_i, \quad i = 1, \dots, \iota \tag{57}$$

Note that for GSA schemes the numerical solution is the same as the last stage value, namely $\bar{f}_{k,i}^{n+1} = \bar{F}_{k,i}^{(\iota)}$. We have the following result

Lemma 1. *If the IMEX method (49)-(50) is of type A and satisfies*

$$\tilde{w}^T = w^T A^{-1} \tilde{A}, \tag{58}$$

then in the limit $\varepsilon \to 0$, it becomes the explicit RK scheme in time characterized by $(\tilde{A}, \tilde{w}, \tilde{c})$ applied to the limit Euler system (6).

Proof. First we rewrite the schemes in compact form, using the vector notation

$$\bar{F}_{k,i} = \bar{f}_{k,i}^n e + \Delta t \tilde{A} \left(\langle L(F_{k,i}) \rangle_x + \frac{\Delta Q(F_{k,i})}{\varepsilon} \right) + \frac{\Delta t}{\varepsilon} A Q(\bar{F}_{k,i}) \tag{59}$$

$$\bar{f}_{k,i}^{n+1} = \bar{f}_{k,i}^n + \Delta t \tilde{w}^T \left(\langle L(F_{k,i}) \rangle_x + \frac{\Delta Q(F_{k,i})}{\varepsilon} \right) + \frac{\Delta t}{\varepsilon} w^T Q(\bar{F}_{k,i}), \tag{60}$$

where we have redefined the source term by $\tilde{Q}(f) = \dfrac{Q(f)}{\varepsilon}$ and we have omitted the tildes, $e = (1, 1, .., 1)^T \in \mathcal{R}^{\iota}$, $\bar{F}_{i,k} = (\bar{F}_{i,k}^{(1)}, \dots, \bar{F}_{i,k}^{(\iota)})^T$, $Q(\bar{F}_{k,i}) = (Q(\bar{F}_{k,i}^{(1)}), \dots, Q(\bar{F}_{k,i}^{(\iota)}))^T$, $\Delta Q(F_{k,i}) = (\Delta Q(F_{k,i}^{(1)}), \dots, \Delta Q(F_{k,i}^{(\iota)}))^T$ and $\langle L(F_{k,i}) \rangle_x = (\langle L(F_{k,i}^{(1)}) \rangle_x, \dots, \langle L(F_{k,i}^{(\iota)}) \rangle_x)$. Now let us rewrite equation (59) in the following form

$$\varepsilon \bar{F}_{k,i} = \varepsilon \bar{f}_{k,i} e + \varepsilon \Delta t \tilde{A} \left(\frac{1}{\varepsilon} \Delta Q(F_{k,i}) + \langle L(F_{k,i}) \rangle_x \right) + \Delta t A Q(\bar{F}_{k,i}). \tag{61}$$

Now by construction A is invertible and thus we can solve for $Q(\bar{F}_{k,i})$ to get

$$\Delta t Q(\bar{F}_{k,i}) = \varepsilon A^{-1}\left(\bar{F}_{k,i} - \bar{f}^n_{k,i} e - \Delta t \tilde{A}\left(\frac{1}{\varepsilon}\Delta Q(F_{k,i}) + \langle L(F_{k,i})\rangle_x\right)\right), \tag{62}$$

and letting $\varepsilon \to 0$ we get

$$Q(\bar{F}_{k,i}) = -A^{-1}\tilde{A}\Delta Q(F_{k,i}). \tag{63}$$

Finally, since $A^{-1}\tilde{A}$ is lower triangular with diagonal elements equal to zero we get

$$Q(\bar{F}^{(l)}_{k,i}) = 0 \quad \Rightarrow \quad \bar{F}^{(l)}_{k,i} = \mathcal{E}_k[\bar{U}^{(l)}_i], \quad l = 1, \dots, \iota. \tag{64}$$

Thus (49)-(50) becomes the explicit Runge-Kutta method applied to the limiting Euler system (6). Let now analyze the behavior of the numerical solution. Inserting (62) into (60) we obtain

$$\bar{f}^{n+1}_{k,i} = \bar{f}^n_{k,i} + \Delta t \tilde{w}^T\left(\langle L(F_{k,i})\rangle_x + \frac{\Delta Q(F_{k,i})}{\varepsilon}\right) + w^T A^{-1}\left(\bar{F}_{k,i} - \bar{f}^n_{k,i} e - \Delta t \tilde{A}\left(\frac{1}{\varepsilon}\Delta Q(F_{k,i}) + \langle L(F_{k,i})\rangle_x\right)\right)$$

which gives

$$\bar{f}^{n+1}_{k,i} = \bar{f}^n_{k,i}\left(1 - w^T A^{-1} e\right) + \Delta t\left(\tilde{w}^T - w^T A^{-1}\tilde{A}\right)\left(\frac{1}{\varepsilon}\Delta Q(F_{k,i}) + \langle L(F_{k,i})\rangle_x\right) + w^T A^{-1} F.$$

Using now the assumption (58) we get

$$\bar{f}^{n+1}_{k,i} = \bar{f}^n_{k,i}\left(1 - w^T A^{-1} e\right) + w^T A^{-1} F, \tag{65}$$

which permits to pass to the limit $\varepsilon \to 0$ in (59)-(60). □

Note that condition (58) is automatically satisfied if the IMEX scheme is GSA. In this case, we have $\bar{f}^{n+1}_{k,i} = \mathcal{E}_k[\bar{U}^{n+1}_i]$ at the discrete level when $\varepsilon \to 0$. Note also that the condition $\tilde{w}^T = w^T A^{-1}\tilde{A}$ is very important since if it is not verified in the limit $\varepsilon \to 0$ the solution blows up.

In the case of IMEX scheme of type CK we have a weaker result. Before addressing this point, we need an additional definition.

Definition 3. The initial data are said to be *consistent* or *well prepared* with the limiting Euler system if

$$f(x, v, t = 0) = M_f(x, v, t = 0) + g^\varepsilon(x, v, t = 0), \qquad \lim_{\varepsilon \to 0} g^\varepsilon(x, v, t = 0) = 0, \tag{66}$$

where the function $g(x, v, t)$ indicates the perturbation from the equilibrium state.

We then have the following Lemma.

Lemma 2. *If the IMEX scheme (49)-(50) is of type CK and GSA then for consistent initial data in the limit $\varepsilon \to 0$ scheme (49)-(50) becomes the explicit RK scheme characterized by $(\tilde{A}, \tilde{w}, \tilde{c})$ applied to the limit Euler system (6).*

Proof. The IMEX scheme can be written as

$$\begin{aligned}
&\bar{F}^{(1)}_{k,i} = \bar{f}^n_{k,i} \\
&\hat{\bar{F}}_{k,i} = \bar{f}^n_{k,i}\hat{e} + \Delta t\tilde{a}\left(\frac{1}{\varepsilon}\Delta Q(F^{(1)}_{k,i}) + \langle L(F^{(1)}_{k,i})\rangle_x\right) + \Delta t\hat{\tilde{A}}\left(\frac{1}{\varepsilon}\Delta Q(\hat{F}_{k,i}) + \langle L(\hat{F}_{k,i})\rangle_x\right) \\
&\qquad + \frac{\Delta t}{\varepsilon} a Q(\bar{F}^{(1)}_{k,i}) + \frac{\Delta t}{\varepsilon}\hat{A} Q(\hat{\bar{F}}_{k,i}),
\end{aligned} \tag{67}$$

$$\begin{aligned}
\bar{f}^{n+1}_{k,i} &= \bar{f}^n + \Delta t\tilde{w}_1\left(\frac{1}{\varepsilon}\Delta Q(F^{(1)}_{k,i}) + \langle L(F^{(1)}_{k,i})\rangle_x\right) + \Delta t\hat{\tilde{w}}^T\left(\frac{1}{\varepsilon}\Delta Q(\hat{F}_{k,i}) + \langle L(\hat{F}_{k,i})\rangle_x\right) \\
&\quad + w_1\frac{\Delta t}{\varepsilon} Q(\bar{F}^{(1)}_{k,i}) + \hat{w}^T\frac{\Delta t}{\varepsilon} Q(\hat{\bar{F}}_{k,i}).
\end{aligned} \tag{68}$$

Solving now, the second equation in (67) for $Q(\hat{\bar{F}}_{k,i})$ we get

$$\Delta t Q(\hat{\bar{F}}_{k,i}) = \varepsilon \hat{A}^{-1}\left[\hat{\bar{F}}_{k,i} - \bar{f}^n_{k,i}\hat{e} - \Delta t \hat{\tilde{A}}\left(\frac{1}{\varepsilon}\Delta Q(\hat{F}_{k,i}) + \langle L(\hat{F}_{k,i})\rangle_x\right) - \Delta t\tilde{a}\left(\frac{1}{\varepsilon}\Delta Q(f^n_{k,i}) + \langle L(f^n_{k,i})\rangle_x\right)\right] - \Delta t \hat{A}^{-1} a Q(\bar{f}^n_{k,i}). \tag{69}$$

As $\varepsilon \to 0$ we obtain

$$Q(\hat{\bar{F}}_{k,i}) = -\hat{A}^{-1}\left(\hat{\tilde{A}}\Delta Q(\hat{F}_{k,i}) + \tilde{a}\Delta Q(f^n_{k,i})\right) - \hat{A}^{-1} a Q(\bar{f}^n_{k,i}). \tag{70}$$

Now since $\bar{f}^n_{k,i}$ is consistent in the limit $\varepsilon \to 0$ we have $\bar{f}^n_{k,i} = \mathcal{E}_k[\bar{U}^n_i]$. This implies that $Q(\bar{f}^n_{k,i}) = 0$ and $\Delta Q(f^n_{k,i}) = 0$ and (70) reduces to

$$Q(\hat{\bar{F}}_{k,i}) = -\hat{A}^{-1}\hat{\tilde{A}}\Delta Q(\hat{F}_{k,i}) \tag{71}$$

which thanks to the fact that $\hat{A}^{-1}\hat{\tilde{A}}$ is lower triangular with zero diagonal elements implies $\hat{\bar{F}}_{k,i} = E_k[\hat{\bar{U}}_i]$. Moreover, since the scheme is GSA, we also have $\bar{f}^{n+1}_{k,i} = E_k[\bar{U}^{n+1}_i]$ and thus at the next time step the initial value remains consistent. Finally, thanks to the projection of the cell averages over the corresponding cell average equilibrium, the moments system obtained from (49)-(50) integrating over the velocity space the cell average distributions corresponds to the explicit Runge-Kutta methods for the Euler equations. □

In the following, we consider three time integration schemes. The first one is the standard first order implicit-explicit Euler scheme for which we do not report the Butcher tableau. The second is the globally second order ARS(2,2,2) [3] scheme

$$\begin{array}{c|ccc} 0 & 0 & 0 & 0 \\ \gamma & \gamma & 0 & 0 \\ 1 & \delta & 1-\delta & 0 \\ \hline & \delta & 1-\delta & 0 \end{array} \qquad \begin{array}{c|ccc} 0 & 0 & 0 & 0 \\ \gamma & 0 & \gamma & 0 \\ 1 & 0 & 1-\gamma & \gamma \\ \hline & 0 & 1-\gamma & \gamma \end{array}$$

with $\gamma = 1 - 1/\sqrt{2}$ and $\delta = 1 - 1/(2\gamma)$, while the third is the globally third order BPR(3,4,3) [12]

$$\begin{array}{c|ccccc} 0 & 0 & 0 & 0 & 0 & 0 \\ 1 & 1 & 0 & 0 & 0 & 0 \\ 2/3 & 4/9 & 2/9 & 0 & 0 & 0 \\ 1 & 1/4 & 0 & 3/4 & 0 & 0 \\ 1 & 1/4 & 0 & 3/4 & 0 & 0 \\ \hline & 1/4 & 0 & 3/4 & 0 & 0 \end{array} \qquad \begin{array}{c|cccccc} 0 & 0 & 0 & 0 & 0 & 0 \\ 1 & 1/2 & 1/2 & 0 & 0 & 0 \\ 2/3 & 5/18 & -1/9 & 1/2 & 0 & 0 \\ 1 & 1/2 & 0 & 0 & 1/2 & 0 \\ 1 & 1/4 & 0 & 3/4 & -1/2 & 1/2 \\ \hline & 1/4 & 0 & 3/4 & -1/2 & 1/2 \end{array}$$

which is fourth order accurate in the implicit part. The three schemes share the common property of being *globally stiffly accurate (GSA)*.

To conclude this part, it remains to discuss the time step limitations. To this aim, we precise that, in all the numerical simulations discussed in the next section, the time step is fixed according to

$$\Delta t = \frac{1}{2}\left(\frac{\Delta x}{\max_{\mathcal{K}}(|v_k|)}\right), \qquad \Delta x = \min_i \sqrt{|P_i|}. \tag{72}$$

In the next Section, we show numerical results which employ the schemes here described.

6. Numerical results

In this section, we show the capability of the class of methods described above to deal with different fluid flows. We start our analysis by performing a set of numerical convergence tests both for the time and the space discretizations. These convergence studies are carried out in different fluid regimes which range from rarefied to dense situations. The second part of this section is devoted to study the behavior of the novel schemes in solving standard benchmark rarefied gas dynamics problems. Finally, the last part is dedicated to applications. We consider the flow around a NACA 0012 airfoil for two different angles of attack and for different values of the Knudsen parameter. This last test case is performed using an MPI parallelization of our algorithm. We stress that this kind of simulations can be performed only thanks to the arbitrarily shaped finite volume approach used, which permits to describe the generic geometry of the airfoil with a high level of details.

Numerical boundary conditions. Due to the finite volume discretization of the transport operator, we rely on standard ghost cell technique for handling numerically the boundary conditions. We distinguish three types of boundary conditions, namely wall, inflow and outflow. According to [5], the ghost state $f_{k,i}^{ghost}$ of cell P_i which is associated to a wall boundary with inward pointing normal n_{ij} is computed as follows:

$$f_{k,i}^{ghost} = \alpha_{k,i}\mathcal{E}_k[U_w], \qquad v_k \cdot n_{ij} > 0, \tag{73}$$

with the accommodation coefficients α obtained in such a way that no mass flux goes across the boundary, i.e.

$$\alpha_{k,i} = -\frac{\sum\limits_{v_k\cdot n_{ij}<0} v_k \cdot n_{ij}\ f_{k,i}^n\,\Delta v}{\sum\limits_{v_k\cdot n_{ij}>0} v_k \cdot n_{ij}\ \mathcal{E}_k[U_w]\,\Delta v}. \tag{74}$$

Here, the wall Maxwellian is given by

$$\mathcal{E}_k[U_w] = \frac{1}{(2\pi\theta)}\exp\left(\frac{-|u_w - v_k|^2}{2\theta}\right), \tag{75}$$

with $u_w = 0$ for no-slip walls and T_w a prescribed temperature of the wall. The quantity $f_{k,i}^n$ denotes the *high order* boundary extrapolated value of the distribution function, that is computed using the CWENO reconstruction polynomial. This easily allows for higher order boundary conditions, since the ghost state is needed at each quadrature point used in the evaluation of the boundary integral for the numerical fluxes in the transport discretization.

Inflow boundary conditions are considered by simply assigning to the ghost cell the upstream Maxwellian distributions $\mathcal{E}_k[U_{in}]$ that have been precomputed according to prescribed values of the macro quantities. For outflow boundaries, upwinding is adopted, therefore the internal state is copied to the ghost cell and the flux computed accordingly.

6.1. Numerical convergence studies

This part is dedicated to the convergence tests. We consider an isentropic vortex test case which has been proposed for the first time in [61] for the Euler equations of compressible gas dynamics. The computational domain is given by the box $\Omega = [0; 10] \times [0; 10]$ with Dirichlet boundary conditions imposed everywhere. A set of non-overlapping polygonal control volumes of characteristic mesh size $h(\Omega) = \sum_i \sqrt{|P_i|}/N_p$ is used to discretize the computational domain, thus allowing the order of convergence to be determined. The velocity space is instead fixed to $\mathcal{V} = [-10; 10] \times [-10; 10]$ and it is paved with a Cartesian grid of 900 equal elements. The initial condition is given by an homogeneous background field which is supplemented with a small perturbation. That is

$$\mathcal{U} = (\rho, u_x, u_y, T) = (1 + \delta\rho, \delta u_x, \delta u_y, \delta T), \tag{76}$$

where the perturbations for temperature δT, density $\delta\rho$ and velocity $(\delta u_x, \delta u_y)$ read

$$\begin{aligned} \delta T &= -\frac{(\gamma-1)\beta^2}{8\gamma\pi^2}e^{1-r^2}, \\ \delta\rho &= (1+\delta T)^{\frac{1}{\gamma-1}} - 1, \\ \begin{pmatrix}\delta u_x \\ \delta u_y\end{pmatrix} &= \frac{\beta}{2\pi}e^{\frac{1-r^2}{2}}\begin{pmatrix}-(y-5)\\ (x-5)\end{pmatrix}. \end{aligned} \tag{77}$$

We set the vortex strength to $\beta = 5$ and the ratio of specific heats $\gamma = d/2 + 1 = 2$ as previously stated according to the governing equations (1). Fig. 5 shows the initial density distribution of this smooth isentropic vortex on a triangular and on a polygonal unstructured mesh, enhancing the versatility of the approach proposed in this work in which simplex elements are nothing but a special case of general polygonal cells.

The errors are measured at the final time t_f in the L_1, L_2 and L_∞ discrete norms for respectively the density and the temperature as follows:

$$L_1 = \int_\Omega \left|\mathcal{U}_{ref}(x,t_f) - \mathcal{U}_h(x,t_f)\right| dxdy, \tag{78}$$

$$L_2 = \sqrt{\int_\Omega \left(\mathcal{U}_{ref}(x,t_f) - \mathcal{U}_h(x,t_f)\right)^2 dxdy}, \tag{79}$$

$$L_\infty = \max_\Omega \left|\mathcal{U}_{ref}(x,t_f) - \mathcal{U}_h(x,t_f)\right|. \tag{80}$$

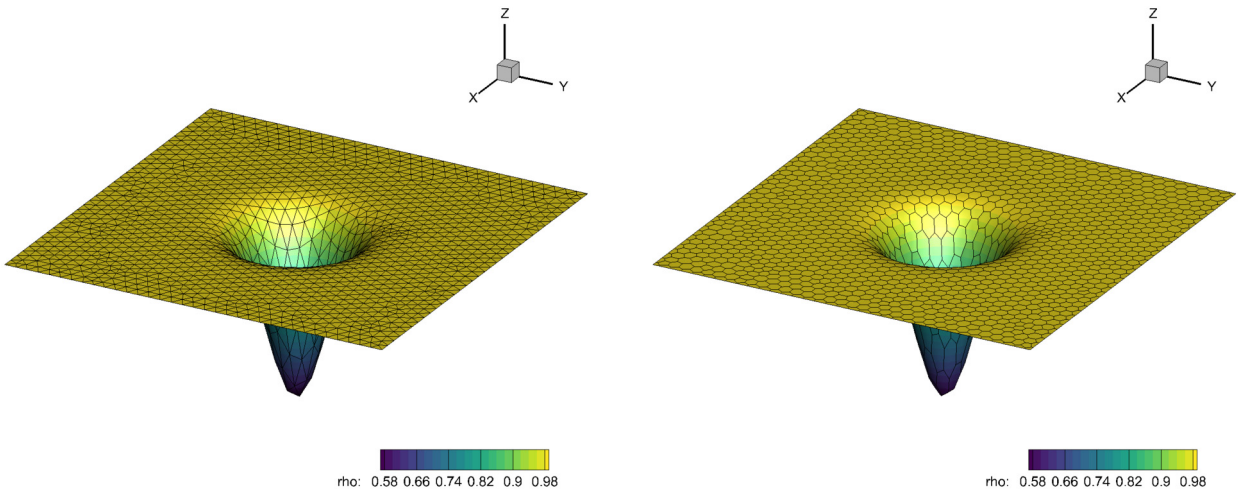

Fig. 5. Initial density distribution of the smooth isentropic vortex on two types of unstructured meshes used for studying the convergence of the CWENO-IMEX schemes. A fourth order CWENO reconstruction has been computed on both triangles and general polygonal cells.

Here, $\mathcal{U}_h(x,t_f)$ represents the high order reconstructed solution for the *macroscopic* quantities obtained with our scheme, while $\mathcal{U}_{ref}(x,t_f)$ is a prescribed *reference solution*. In the sequel, we measure three different kinds of convergence, namely convergence in (i) space, (ii) space-time and (iii) time discretization. More in details:

- If we operate in the stiff limit $\varepsilon \to 0$ the reference solution is the exact solution, i.e. $\mathcal{U}_{ref}(x,t_f) = \mathcal{U}_e(x,t_f)$, which is given by the initial condition. In this situation, we consider a *space-time* measure of the error. Then, both a single space and a fully space-time convergence study are performed with the space-time convergence rates $\mathrm{p}_k^{L_s}(\Delta x, \Delta t)$ for the generic norm L_s $(s = 1, 2, \infty)$ computed as

$$\mathrm{p}_k^{L_s}(\Delta x, \Delta t) = \frac{\log\left(\frac{L_{s,k-1}}{L_{s,k}}\right)}{\log\left(\frac{h_{k-1}}{h_k}\right)}. \tag{81}$$

  Here, h_{k-1} and h_k represent two characteristic mesh sizes such that $h_k < h_{k-1}$.
- If $\varepsilon \neq 0$, no analytical solution is available, hence convergence rates can only be extrapolated numerically. Therefore, a *fixed* discretization in both physical and phase-space is kept, while performing a time stepping refinement in order to properly check the time accuracy of the algorithm. Specifically, the reference solution is given by the numerical solution $\mathcal{U}_{h_t}(x,t_f)$ that has been computed with a smaller time step Δt_k, i.e. $\Delta t_k < \Delta t_{k-1}$, thus $\mathcal{U}_{ref}(x,t_f) = \mathcal{U}_{h_t}(x,t_f)$. In this case, a *time* measure of the error is considered, hence a time convergence study is performed. The time step is halved at each level of refinement, so that the evaluation of the time convergence rates $\mathrm{p}_k^{L_s}(\Delta t)$ for the generic norm L_s $(s = 1, 2, \infty)$ writes

$$\mathrm{p}_k^{L_s}(\Delta t) = \log_2\left(\frac{L_{s,k-1}}{L_{s,k}}\right). \tag{82}$$

The first analysis we perform consists in the verification of the high order CWENO reconstruction presented in Section 4.2. In order to carry out this analysis, a sequence of four *triangular* grids with characteristic mesh size $h(\Omega)$ is used to compute the convergence of the spatial reconstruction at the final time $t_f = 0$, that is no time evolution is performed. The results are presented in Table 2 which clearly show convergence from first up to fourth order of accuracy in space. In other words, we check that the macroscopic variables are approximated with the correct order of accuracy by the reconstruction $f_{i,k}(x,t)$ of (32). Successively, we perform a space-time numerical convergence on polygonal meshes for the case in which the Knudsen number is set to zero, i.e. in the fluid limit $\varepsilon = 0$. The results of this test are shown in Table 3 where the formal order of convergence depending on the employed CWENO-IMEX scheme (one, two or three) is found at time $t_f = 0.1$. Table 4 for $\varepsilon = 10^{-3}$, 5 for $\varepsilon = 10^{-2}$ and 6 for $\varepsilon = 1$ show instead that the theoretical time accuracy is reached for the different flow regimes at the final time $t_f = 9 \cdot 10^{-3}$ when the flow is out of equilibrium. Again in these cases, the order one, two and three is achieved according to the choice of the IMEX scheme. Resuming, Table 2 demonstrates that the formal order of accuracy is obtained in space, while Tables 4, 5 and 6 show the achievement of the formal accuracy in time. Fully space-time convergences are then highlighted in Table 3, where the results confirm that the novel CWENO-IMEX schemes are up to third order accurate in both space and time. The details of the discretizations used in space and time for each convergence test are conveniently summarized by Table 1.

Table 1
Setting of the discretization used for the convergence analysis in space, space-time and time of the novel CWENO-IMEX schemes.

	Space test (Table 2)	Space-time test (Table 3)	Time test (Tables 4-6)	
Mesh type	Triangular	Polygonal	Polygonal	
Refinement level	# elements N_p	# elements N_p	# elements N_p	time step Δt
1	1298	667	1465	$1.80 \cdot 10^{-3}$
2	2292	2570	1465	$9.00 \cdot 10^{-4}$
3	5180	5707	1465	$4.50 \cdot 10^{-4}$
4	9192	10118	1465	$2.25 \cdot 10^{-4}$

Table 2
Numerical convergence results for the BGK model using the CWENO reconstruction from first up to fourth order of accuracy on a sequence of refined triangular meshes of size $h(\Omega)$. The errors are measured in L_1, L_2 and L_∞ norm and refer to the variables ρ (density) and T (temperature).

CWENO $O1$

$h(\Omega)$	ρ_{L_1}	$O(\rho_{L_1})$	ρ_{L_2}	$O(\rho_{L_2})$	ρ_{L_∞}	ρ_{L_∞}
2.77E-01	1.292E-01	-	4.606E-02	-	3.287E-02	-
2.09E-01	9.404E-02	1.1	3.317E-02	1.2	2.356E-02	1.2
1.39E-01	6.355E-01	1.0	2.253E-02	0.9	1.774E-02	0.7
1.04E-01	4.725E-02	1.0	1.684E-02	1.0	1.330E-02	1.0
$h(\Omega)$	T_{L_1}	$O(T_{L_1})$	T_{L_2}	$O(T_{L_2})$	T_{L_∞}	T_{L_∞}
2.77E-01	8.405E-01	-	2.185E-01	-	2.105E-01	-
2.09E-01	6.197E-01	1.1	1.581E-01	1.1	1.353E-01	1.6
1.39E-01	4.142E-01	1.0	1.068E-01	1.0	9.726E-02	0.8
1.04E-01	3.102E-01	1.0	8.027E-02	1.0	7.247E-02	1.0

CWENO $O2$

$h(\Omega)$	ρ_{L_1}	$O(\rho_{L_1})$	ρ_{L_2}	$O(\rho_{L_2})$	ρ_{L_∞}	ρ_{L_∞}
2.77E-01	3.909E-02	-	1.603E-02	-	2.421E-02	-
2.09E-01	2.060E-02	2.3	8.391E-03	2.3	1.450E-02	1.8
1.39E-01	9.621E-03	1.9	4.008E-03	1.8	9.432E-03	1.1
1.04E-01	5.529E-03	1.9	2.370E-03	1.8	5.684E-03	1.8
$h(\Omega)$	T_{L_1}	$O(T_{L_1})$	T_{L_2}	$O(T_{L_2})$	T_{L_∞}	T_{L_∞}
2.77E-01	2.395E-01	-	7.922E-02	-	1.237E-01	-
2.09E-01	1.300E-01	2.1	4.216E-02	2.2	7.788E-02	1.6
1.39E-01	5.912E-02	1.9	1.962E-02	1.9	3.251E-02	2.1
1.04E-01	3.292E-02	2.0	1.090E-02	2.0	2.287E-02	1.2

CWENO $O3$

$h(\Omega)$	ρ_{L_1}	$O(\rho_{L_1})$	ρ_{L_2}	$O(\rho_{L_2})$	ρ_{L_∞}	ρ_{L_∞}
2.77E-01	1.947E-02	-	7.999E-03	-	1.260E-02	-
2.09E-01	7.723E-03	3.3	3.053E-03	3.4	5.167E-03	3.1
1.39E-01	2.417E-03	2.9	9.909E-04	2.8	1.798E-03	2.6
1.04E-01	1.027E-03	3.0	4.224E-04	3.0	7.479E-04	3.1
$h(\Omega)$	T_{L_1}	$O(T_{L_1})$	T_{L_2}	$O(T_{L_2})$	T_{L_∞}	T_{L_∞}
2.77E-01	1.160E-01	-	4.160E-02	-	8.602E-02	-
2.09E-01	4.632E-02	3.2	1.154E-02	3.5	2.781E-02	4.0
1.39E-01	1.449E-02	2.9	5.062E-03	2.7	9.305E-03	2.7
1.04E-01	6.139E-03	3.0	2.116E-03	3.0	4.549E-03	2.5

CWENO $O4$

$h(\Omega)$	ρ_{L_1}	$O(\rho_{L_1})$	ρ_{L_2}	$O(\rho_{L_2})$	ρ_{L_∞}	ρ_{L_∞}
2.77E-01	7.722E-03	-	3.128E-03	-	7.870E-03	-
2.09E-01	2.373E-03	4.2	9.098E-04	4.3	2.069E-03	4.7
1.39E-01	4.790E-03	3.9	1.900E-04	3.8	5.403E-04	3.3
1.04E-01	1.397E-03	4.3	5.249E-05	4.5	1.492E-04	4.5
$h(\Omega)$	T_{L_1}	$O(T_{L_1})$	T_{L_2}	$O(T_{L_2})$	T_{L_∞}	T_{L_∞}
2.77E-01	4.873E-02	-	1.932E-02	-	7.623E-02	-
2.09E-01	1.377E-02	4.4	4.870E-03	4.8	1.416E-02	5.9
1.39E-01	2.920E-03	3.8	1.090E-03	3.7	3.262E-03	3.6
1.04E-01	8.754E-04	4.2	3.227E-04	4.2	1.191E-03	3.5

Table 3
Numerical convergence results for the BGK model using CWENO-IMEX schemes from first up to third order at time $t_f = 0.1$ with $Kn = 0$ on a sequence of refined polygonal meshes of size $h(\Omega)$. The errors are measured in L_1, L_2 and L_∞ norm and refer to the variables ρ (density) and T (temperature).

CWENO-IMEX $O1$ $Kn = 0$

$h(\Omega)$	ρ_{L_1}	$O(\rho_{L_1})$	ρ_{L_2}	$O(\rho_{L_2})$	ρ_{L_∞}	ρ_{L_∞}
3.83E-01	2.291E-01	-	8.151E-02	-	6.465E-02	-
1.96E-01	1.157E-01	1.0	4.137E-02	1.0	3.357E-02	1.0
1.32E-01	7.757E-02	1.0	2.769E-02	1.0	2.242E-02	1.0
9.90E-02	5.828E-02	1.0	2.087E-02	1.0	2.002E-02	0.4
$h(\Omega)$	T_{L_1}	$O(T_{L_1})$	T_{L_2}	$O(T_{L_2})$	T_{L_∞}	T_{L_∞}
3.83E-01	5.073E-01	-	1.769E-01	-	1.657E-01	-
1.96E-01	2.611E-01	1.0	9.170E-02	1.0	8.827E-02	0.9
1.32E-01	1.756E-01	1.0	6.170E-02	1.0	5.947E-02	1.0
9.90E-02	1.325E-01	1.0	4.682E-02	1.0	5.296E-02	0.4

CWENO-IMEX $O2$ $Kn = 0$

$h(\Omega)$	ρ_{L_1}	$O(\rho_{L_1})$	ρ_{L_2}	$O(\rho_{L_2})$	ρ_{L_∞}	ρ_{L_∞}
3.83E-01	5.721E-02	-	2.278E-02	-	2.991E-02	-
1.96E-01	1.087E-02	2.5	4.099E-03	2.6	6.541E-03	2.3
1.32E-01	4.214E-03	2.4	1.458E-03	2.6	2.239E-03	2.7
9.90E-02	2.224E-03	2.2	7.589E-04	2.3	1.512E-03	1.4
$h(\Omega)$	T_{L_1}	$O(T_{L_1})$	T_{L_2}	$O(T_{L_2})$	T_{L_∞}	T_{L_∞}
3.83E-01	1.852E-01	-	6.593E-02	-	7.779E-02	-
1.96E-01	3.390E-02	2.5	1.231E-02	2.5	1.574E-02	2.4
1.32E-01	1.179E-02	2.7	4.244E-03	2.7	7.824E-03	1.8
9.90E-02	5.929E-03	2.4	2.102E-03	2.5	3.121E-03	3.2

CWENO-IMEX $O3$ $Kn = 0$

$h(\Omega)$	ρ_{L_1}	$O(\rho_{L_1})$	ρ_{L_2}	$O(\rho_{L_2})$	ρ_{L_∞}	ρ_{L_∞}
3.83E-01	6.270E-02	-	2.535E-02	-	3.247E-02	-
1.96E-01	1.052E-02	2.7	4.489E-03	2.6	7.139E-03	2.3
1.32E-01	3.154E-03	3.0	1.329E-03	3.1	2.244E-03	2.9
9.90E-02	1.337E-03	3.0	5.541E-04	3.1	1.061E-03	2.6
$h(\Omega)$	T_{L_1}	$O(T_{L_1})$	T_{L_2}	$O(T_{L_2})$	T_{L_∞}	T_{L_∞}
3.83E-01	2.183E-01	-	7.634E-02	-	9.801E-02	-
1.96E-01	3.699E-02	2.7	1.365E-02	2.6	1.579E-02	2.7
1.32E-01	1.090E-02	3.1	3.988E-03	3.1	6.472E-03	2.2
9.90E-02	4.442E-03	3.1	1.620E-03	3.1	2.139E-03	3.9

6.2. Lax problem

In this part, we consider a classical Lax shock tube Riemann problem. This class of problems are widely adopted to validate numerical algorithms for the solution of the compressible Euler equations. Here, we consider the case in which fluid equations are valid and the case in which flow is rarefied and the solution departs from the standard left-propagating rarefaction wave, the intermediate contact discontinuity and the right-propagating shock wave. The essential feature one can observe in rarefied flows is the presence of a physical diffusion which mitigates the waves making the solution smooth. This kind of tests are interesting because they allow the approximation of a large suite of hyperbolic waves to be properly checked and, though intrinsically one-dimensional, they are absolutely non-trivial and multidimensional when applied to unstructured meshes, where in general the element edges are not aligned with the fluid motion.

The computational domain is the box $\Omega = [-1; 1] \times [-0.05; 0.05]$, that is discretized with a total number of $[100 \times 10]$ triangular control volumes with characteristic mesh size of $h(\Omega) = 0.02$. Periodic boundary conditions are set in y-direction, while Dirichlet boundaries are imposed in the x-direction. The velocity space $\mathcal{V} = [-15; 15] \times [-15; 15]$ counts a total number of $32 \times 32 = 1024$ regular Cartesian control volumes. The initial condition is given in terms of primitive variables $\mathcal{U} = (\rho, u_x, u_y, T)$ and consists of two states, namely the left $\mathcal{U}_L$ and the right $\mathcal{U}_R$ state, that are separated at $x_D = 0$:

$$\mathcal{U}_L = \left(0.445, 0.698, 0, \frac{3.528}{\rho_L}\right), \qquad \mathcal{U}_R = \left(0.5, 0, 0, \frac{0.571}{\rho_R}\right). \tag{83}$$

The fully third order CWENO-IMEX scheme for running the Lax problem until the final time $t_f = 0.1$ is employed with different values of the Knudsen number. Specifically, Fig. 6 shows the density distribution as well as a one dimensional cut along the x-axis with 200 points for density, horizontal velocity and temperature with $\varepsilon = 5 \cdot 10^{-5}$. Similar images have been obtained for $\varepsilon = 5 \cdot 10^{-4}$ in Fig. 7 and $\varepsilon = 5 \cdot 10^{-3}$ in Fig. 8. The numerical results are compared against a reference solution that has been obtained using the same IMEX Runge-Kutta method and a one-dimensional in space second order

Table 4
Numerical convergence results for the BGK model using CWENO-IMEX schemes from first up to third order at time $t_f = 0.009$ with $Kn = 10^{-3}$ on a polygonal mesh with characteristic mesh size $h = 1/3$. The errors are measured in L_1, L_2 and L_∞ norm and refer to the variables ρ (density) and T (temperature).

CWENO-IMEX $\mathcal{O}1$ $Kn = 10^{-3}$

Δt	ρ_{L_1}	$\mathcal{O}(\rho_{L_1})$	ρ_{L_2}	$\mathcal{O}(\rho_{L_2})$	ρ_{L_∞}	ρ_{L_∞}
1.80E-03	-	-	-	-	-	-
9.00E-04	7.723E-06	-	2.376E-06	-	2.148E-06	-
4.50E-04	3.917E-06	1.0	1.204E-06	1.0	1.088E-06	1.0
2.25E-04	1.971E-06	1.0	6.059E-07	1.0	5.468E-07	1.0
Δt	T_{L_1}	$\mathcal{O}(T_{L_1})$	T_{L_2}	$\mathcal{O}(T_{L_2})$	T_{L_∞}	T_{L_∞}
1.80E-03	-	-	-	-	-	-
9.00E-04	1.842E-05	-	5.162E-06	-	6.830E-06	-
4.50E-04	9.270E-06	1.0	2.591E-06	1.0	3.374E-06	1.0
2.25E-04	4.649E-06	1.0	1.298E-06	1.0	1.677E-06	1.0

CWENO-IMEX $\mathcal{O}2$ $Kn = 10^{-3}$

Δt	ρ_{L_1}	$\mathcal{O}(\rho_{L_1})$	ρ_{L_2}	$\mathcal{O}(\rho_{L_2})$	ρ_{L_∞}	ρ_{L_∞}
1.80E-03	-	-	-	-	-	-
9.00E-04	3.158E-07	-	1.345E-07	-	2.398E-07	-
4.50E-04	8.461E-08	1.9	3.427E-08	2.0	5.775E-08	2.1
2.25E-04	2.189E-08	2.0	8.627E-09	2.0	1.406E-08	2.0
Δt	T_{L_1}	$\mathcal{O}(T_{L_1})$	T_{L_2}	$\mathcal{O}(T_{L_2})$	T_{L_∞}	T_{L_∞}
1.80E-03	-	-	-	-	-	-
9.00E-04	1.406E-06	-	4.814E-07	-	7.775E-07	-
4.50E-04	3.666E-07	1.9	1.231E-07	2.0	1.995E-07	2.0
2.25E-04	9.359E-08	2.0	3.103E-08	2.0	4.996E-08	2.0

CWENO-IMEX $\mathcal{O}3$ $Kn = 10^{-3}$

Δt	ρ_{L_1}	$\mathcal{O}(\rho_{L_1})$	ρ_{L_2}	$\mathcal{O}(\rho_{L_2})$	ρ_{L_∞}	ρ_{L_∞}
2.25E-04	-	-	-	-	-	-
1.12E-05	2.017E-07	-	8.656E-08	-	1.921E-07	-
5.62E-05	3.816E-08	2.4	1.511E-08	2.5	3.067E-08	2.6
2.81E-05	6.212E-09	2.6	2.353E-09	2.7	4.513E-09	2.8
Δt	T_{L_1}	$\mathcal{O}(T_{L_1})$	T_{L_2}	$\mathcal{O}(T_{L_2})$	T_{L_∞}	T_{L_∞}
2.25E-04	-	-	-	-	-	-
1.12E-05	7.263E-07	-	2.614E-07	-	4.837E-07	-
5.62E-05	1.389E-07	2.4	4.683E-08	2.5	8.381E-08	2.5
2.81E-05	2.274E-08	2.6	7.362E-09	2.7	1.274E-08	2.7

WENO scheme for the transport part on a very fine Cartesian grid composed by 1000 cells. The results show a perfect matching between the solutions for each stiffness setting, thus validating the approach here proposed.

6.3. Explosion problem

The explosion problem can be seen as a multidimensional extension of the classical Sod shock tube test case. The computational domain is the square of dimension $\Omega = [-1; 1] \times [-1; 1]$, and the initial condition is composed of two different states $(\mathcal{U}_L, \mathcal{U}_R)$, separated by a discontinuity at radius $R_d = 0.5$:

$$\begin{cases} \mathcal{U}_L = \left(1, 0, 0, \frac{1}{R\,\rho_L}\right) & r \le R_d, \\ \mathcal{U}_R = \left(0.125, 0, 0, \frac{0.1}{R\,\rho_R}\right) & r > R_d, \end{cases} \tag{84}$$

with the radial position $r = \sqrt{x^2 + y^2}$. The spatial domain is discretized by $N_p = 35186$ Voronoi elements with characteristic mesh size $h = 1/75$, while the velocity space is composed of 1024 Cartesian cells ranging in the interval $[-15; 15] \times [-15; 15]$. More than 300 million space-time degrees of freedom are thus involved by this simulation. The final time is chosen to be $t_f = 0.07$, so that the shock wave does not cross the external boundary of the domain, where a transmissive boundary condition is set. The numerical results have been computed using the third order version of the CWENO-IMEX schemes presented in this work, and they are depicted in Fig. 9 for Knudsen number $\varepsilon = 5 \cdot 10^{-5}$, $\varepsilon = 5 \cdot 10^{-4}$ and $\varepsilon = 5 \cdot 10^{-3}$. Furthermore, the reference solution of the Euler equations, obtained as detailed in [14,93], is plot as well in order to appreciate the convergence towards the fluid regime in the stiff limit. The results show a 1D cut along the x-axis with 200 points for density, horizontal velocity and temperature as well as a three-dimensional view of the density distribution.

Table 5
Numerical convergence results for the BGK model using CWENO-IMEX schemes from first up to third order at time $t_f = 0.009$ with $Kn = 10^{-2}$ on a polygonal mesh with characteristic mesh size $h = 1/3$. The errors are measured in L_1, L_2 and L_∞ norm and refer to the variables ρ (density) and T (temperature).

CWENO-IMEX $\mathcal{O}1$ $Kn = 10^{-2}$

Δt	ρ_{L_1}	$\mathcal{O}(\rho_{L_1})$	ρ_{L_2}	$\mathcal{O}(\rho_{L_2})$	ρ_{L_∞}	ρ_{L_∞}
1.80E-03	-	-	-	-	-	-
9.00E-04	5.071E-06	-	1.494E-06	-	2.066E-06	-
4.50E-04	2.537E-06	1.0	7.455E-07	1.0	1.025E-06	1.0
2.25E-04	1.269E-06	1.0	3.724E-07	1.0	5.108E-07	1.0
Δt	T_{L_1}	$\mathcal{O}(T_{L_1})$	T_{L_2}	$\mathcal{O}(T_{L_2})$	T_{L_∞}	T_{L_∞}
1.80E-03	-	-	-	-	-	-
9.00E-04	1.707E-05	-	4.356E-06	-	6.788E-06	-
4.50E-04	8.766E-06	1.0	2.204E-06	1.0	3.355E-06	1.0
2.25E-04	4.448E-06	1.0	1.109E-06	1.0	1.668E-06	1.0

CWENO-IMEX $\mathcal{O}2$ $Kn = 10^{-2}$

Δt	ρ_{L_1}	$\mathcal{O}(\rho_{L_1})$	ρ_{L_2}	$\mathcal{O}(\rho_{L_2})$	ρ_{L_∞}	ρ_{L_∞}
1.80E-03	-	-	-	-	-	-
9.00E-04	1.751E-07	-	7.856E-08	-	1.753E-07	-
4.50E-04	4.333E-08	2.0	1.949E-08	2.0	4.440E-08	2.0
2.25E-04	1.078E-08	2.0	4.856E-09	2.0	1.117E-08	2.0
Δt	T_{L_1}	$\mathcal{O}(T_{L_1})$	T_{L_2}	$\mathcal{O}(T_{L_2})$	T_{L_∞}	T_{L_∞}
1.80E-03	-	-	-	-	-	-
9.00E-04	6.487E-07	-	2.129E-07	-	3.008E-07	-
4.50E-04	1.621E-07	2.0	5.322E-08	2.0	7.520E-08	2.0
2.25E-04	4.063E-08	2.0	1.329E-08	2.0	1.872E-08	2.0

CWENO-IMEX $\mathcal{O}3$ $Kn = 10^{-2}$

Δt	ρ_{L_1}	$\mathcal{O}(\rho_{L_1})$	ρ_{L_2}	$\mathcal{O}(\rho_{L_2})$	ρ_{L_∞}	ρ_{L_∞}
1.80E-03	-	-	-	-	-	-
9.00E-04	2.776E-08	-	1.138E-08	-	1.936E-09	-
4.50E-04	3.654E-09	2.9	1.494E-09	2.9	2.533E-09	2.9
2.25E-04	4.695E-10	3.0	1.916E-10	3.0	3.243E-10	3.0
Δt	T_{L_1}	$\mathcal{O}(T_{L_1})$	T_{L_2}	$\mathcal{O}(T_{L_2})$	T_{L_∞}	T_{L_∞}
1.80E-03	-	-	-	-	-	-
9.00E-04	7.443E-08	-	2.881E-08	-	4.487E-08	-
4.50E-04	9.941E-09	2.9	3.800E-09	2.9	5.915E-09	2.9
2.25E-04	1.287E-09	2.9	4.888E-10	3.0	7.606E-10	3.0

Notice that the solution exhibits excellent symmetry properties, which is not obvious due to the usage of an unstructured computational grid.

6.4. Fluid flow around NACA 0012 airfoil

Finally, as a last example we consider a problem closer to the physical reality. The aim of this test case is only to show the capability of the scheme to handle more complex geometries and real world phenomena, without analyzing any quantitative detail. We employ again our CWENO-IMEX scheme on unstructured grids to study the flow around a NACA 0012 airfoil profile for different rarefied regimes. The airfoil is embedded in a computational domain $\Omega = [-5; 10] \times [-4; 4]$, that is paved with $N_p = 6554$ Voronoi control volumes in space. Two different angles of attack α of the airfoil are simulated, namely $\alpha = 0$ and $\alpha = 20$, as shown in Fig. 10. A constant density $\rho_0 = 1$ is initially assigned to the fluid with a velocity field $(u_x(t = 0), u_y(t = 0) = (15, 0)$. The ratio of specific heats is chosen to be $\gamma = 1.4$, so that the initial pressure reads $p_0 = 100/\gamma$ and the initial temperature is given by $T = \dfrac{p_0}{\rho_0}$. The sound speed is computed as $c = \sqrt{\gamma T} = 10$ and the Mach number of the flow results to be $M = 1.5$, hence a supersonic regime is considered. Two different settings are presented: the first scenario deals with a Knudsen number $\varepsilon_1 = 10^{-4}$, while we set $\varepsilon_2 = 5 \cdot 10^{-3}$ for the second simulation. The velocity space is defined by the Cartesian domain $[-60; 60] \times [-60; 60]$, which is discretized using a grid composed of 40×40 control volumes. The third order version of CWENO-IMEX schemes is adopted for running the simulations up to the final time $t = 0.5$. Thus, the simulation size counts more than 100 million space-time degrees of freedom. For qualitative comparison purposes, the same simulations are also performed employing the compressible Navier-Stokes equations. Although the two models are different, the corresponding physical viscosity μ can be estimated as

Table 6
Numerical convergence results for the BGK model using CWENO-IMEX schemes from first up to third order at time $t_f = 0.009$ with $Kn = 10^0$ on a polygonal mesh with characteristic mesh size $h = 1/3$. The errors are measured in L_1, L_2 and L_∞ norm and refer to the variables ρ (density) and T (temperature).

CWENO-IMEX $O1$ $Kn = 10^0$

Δt	ρ_{L_1}	$O(\rho_{L_1})$	ρ_{L_2}	$O(\rho_{L_2})$	ρ_{L_∞}	ρ_{L_∞}
1.80E-03	-	-	-	-	-	-
9.00E-04	4.037E-06	-	1.192E-06	-	2.002E-06	-
4.50E-04	2.007E-06	1.0	5.913E-07	1.0	9.900E-07	1.0
2.25E-04	1.000E-06	1.0	2.944E-07	1.0	4.923E-07	1.0
Δt	T_{L_1}	$O(T_{L_1})$	T_{L_2}	$O(T_{L_2})$	T_{L_∞}	T_{L_∞}
1.80E-03	-	-	-	-	-	-
9.00E-04	2.083E-05	-	5.079E-06	-	6.727E-06	-
4.50E-04	1.038E-05	1.0	2.526E-06	1.0	3.319E-06	1.0
2.25E-04	5.184E-06	1.0	1.259E-06	1.0	1.648E-06	1.0

CWENO-IMEX $O2$ $Kn = 10^0$

Δt	ρ_{L_1}	$O(\rho_{L_1})$	ρ_{L_2}	$O(\rho_{L_2})$	ρ_{L_∞}	ρ_{L_∞}
1.80E-03	-	-	-	-	-	-
9.00E-04	8.169E-08	-	4.431E-08	-	1.651E-07	-
4.50E-04	2.020E-08	2.0	1.096E-08	2.0	4.082E-08	2.0
2.25E-04	5.025E-09	2.0	2.726E-09	2.0	1.015E-08	2.0
Δt	T_{L_1}	$O(T_{L_1})$	T_{L_2}	$O(T_{L_2})$	T_{L_∞}	T_{L_∞}
1.80E-03	-	-	-	-	-	-
9.00E-04	2.233E-07	-	9.544E-08	-	1.816E-07	-
4.50E-04	5.525E-08	2.0	2.361E-08	2.0	4.459E-08	2.0
2.25E-04	1.374E-08	2.0	5.873E-09	2.0	1.106E-08	2.0

CWENO-IMEX $O3$ $Kn = 10^0$

Δt	ρ_{L_1}	$O(\rho_{L_1})$	ρ_{L_2}	$O(\rho_{L_2})$	ρ_{L_∞}	ρ_{L_∞}
1.80E-03	-	-	-	-	-	-
9.00E-04	1.458E-09	-	6.453E-10	-	1.732E-09	-
4.50E-04	1.785E-10	3.0	7.903E-11	3.0	2.130E-10	3.0
2.25E-04	2.213E-11	3.0	9.783E-12	3.0	2.643E-11	3.0
Δt	T_{L_1}	$O(T_{L_1})$	T_{L_2}	$O(T_{L_2})$	T_{L_∞}	T_{L_∞}
1.80E-03	-	-	-	-	-	-
9.00E-04	5.476E-09	-	2.411E-09	-	5.982E-09	-
4.50E-04	6.695E-10	3.0	2.943E-10	3.0	7.353E-10	3.0
2.25E-04	8.281E-11	3.0	3.637E-11	3.0	9.120E-11	3.0

$$\mu = \varepsilon \, \rho \, T, \tag{85}$$

thus obtaining $\mu_1 = 7.142857 \cdot 10^{-3}$ and $\mu_2 = 3.571459 \cdot 10^{-1}$, respectively. The associated Reynolds numbers are $Re_1 = 2100$ and $Re_2 = 42$. The results obtained for the Navier-Stokes model are computed using the same computational grid and relying on the same third order CWENO reconstruction technique, while the ADER paradigm allows for achieving third order time stepping, following [55]. Notice that one could directly use the expression (85) to define the collision operator in the BGK model, however we limit ourselves to adopt the choice $\nu = \rho$ as done for all the other test cases presented in this work.

Figs. 11 and 12 depict the results computed for the airfoil with angle of attack $\alpha = 0$ with $\varepsilon_1 = 10^{-4}$ and $\varepsilon_2 = 5 \cdot 10^{-3}$ respectively. Specifically, we show the density, the absolute value of the velocity and the temperature contours for BGK (left column) and for compressible Navier-Stokes (right column) models. We use 30 contour levels in the range $[0.45; 2.35]$ for density, $[1; 15]$ for velocity magnitude and $[65; 105]$ for temperature. Results for $\alpha = 20$ are then shown in Figs. 13-14, where one can appreciate a qualitative agreement between the two models, especially in the case with $\varepsilon_1 = 10^{-4}$. Different patterns for the shock wave can be seen, as well as the differences in temperature distribution are notable between the different Knudsen numbers, as expected.

The results shown in this part represent a first example of what can be studied with such high order method on unstructured meshes. We postpone to future investigations a detailed study of the flow around airfoils with kinetic equations in which the drag and lift coefficients can be measured in details and compared with other numerical methods for conservation laws, highlighting the limits of the fluid models.

6.5. Profiling

The code is written in `Fortran` language and parallelized using the standard MPI library. The physical space is partitioned among different CPUs, while keeping the velocity space copied within each thread. The first step in the algorithm

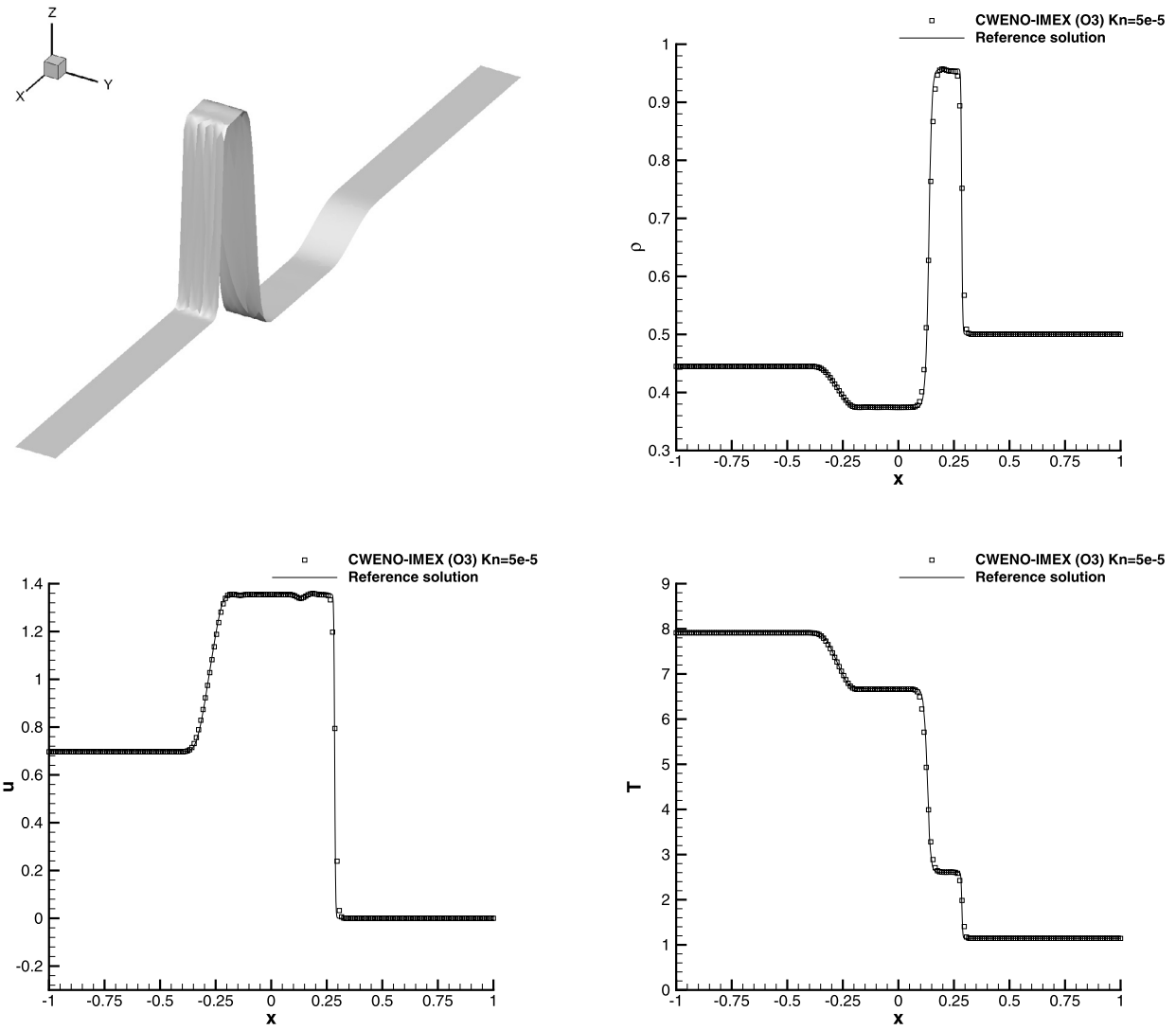

Fig. 6. Lax shock tube problem with $Kn = 5 \cdot 10^{-5}$ at time $t_f = 0.1$. Three dimensional view of density profile together with a 1D cut along the x-axis through the third order numerical results and comparison with exact solution for density, velocity in the x-direction and temperature.

is given by the generation of the computational grid, which is carried out as follows. The free graph partitioning software Metis/ParMetis [71] is applied to a primary *coarse* mesh made of simplex control volumes. Next, each thread performs a *local* isotropic mesh refinement, thus each coarse triangular element is subdivided into a total number of $N_T = \chi^2$ sub-triangles, with χ being a refinement factor which can be arbitrarily chosen. In order to generate a sufficiently extended layer of ghost cells needed for the numerical flux computation, each CPU produces also the fine sub-elements for all Voronoi neighbors of its own elements. Finally, the dual polygonal mesh is built fully in parallel by each thread *separately*, thus saving memory and exploiting the MPI architecture of non-shared memory. Such technique has also been used in the context of multidimensional simplex meshes [45] achieving the generation of a grid composed of one billion of tetrahedra. Notice that the choice of the CWENO strategy is particularly well-suited because all one-sided reconstruction stencils only involve the first layer of Voronoi neighbors of an element. Therefore, this is enough to ensure a proper accomplishment of the reconstruction step even on MPI locally partitioned meshes. This would not be true in the case of standard WENO algorithms, where the lateral stencils are composed of much more elements depending on the reconstruction degree M, hence imposing a larger layer of ghost cells to be built and exchanged among different threads. In our approach the final computational grid is *never* fully assembled, but each CPU only accounts for its partition supplemented with the required ghost cells.

Regarding the MPI communications needed while performing one time step of the numerical scheme, only the cell averages of the distribution functions must be exchanged before the CWENO reconstruction is carried out. Therefore, the number of stages in the IMEX time stepping determines the number of MPI communications that are needed.

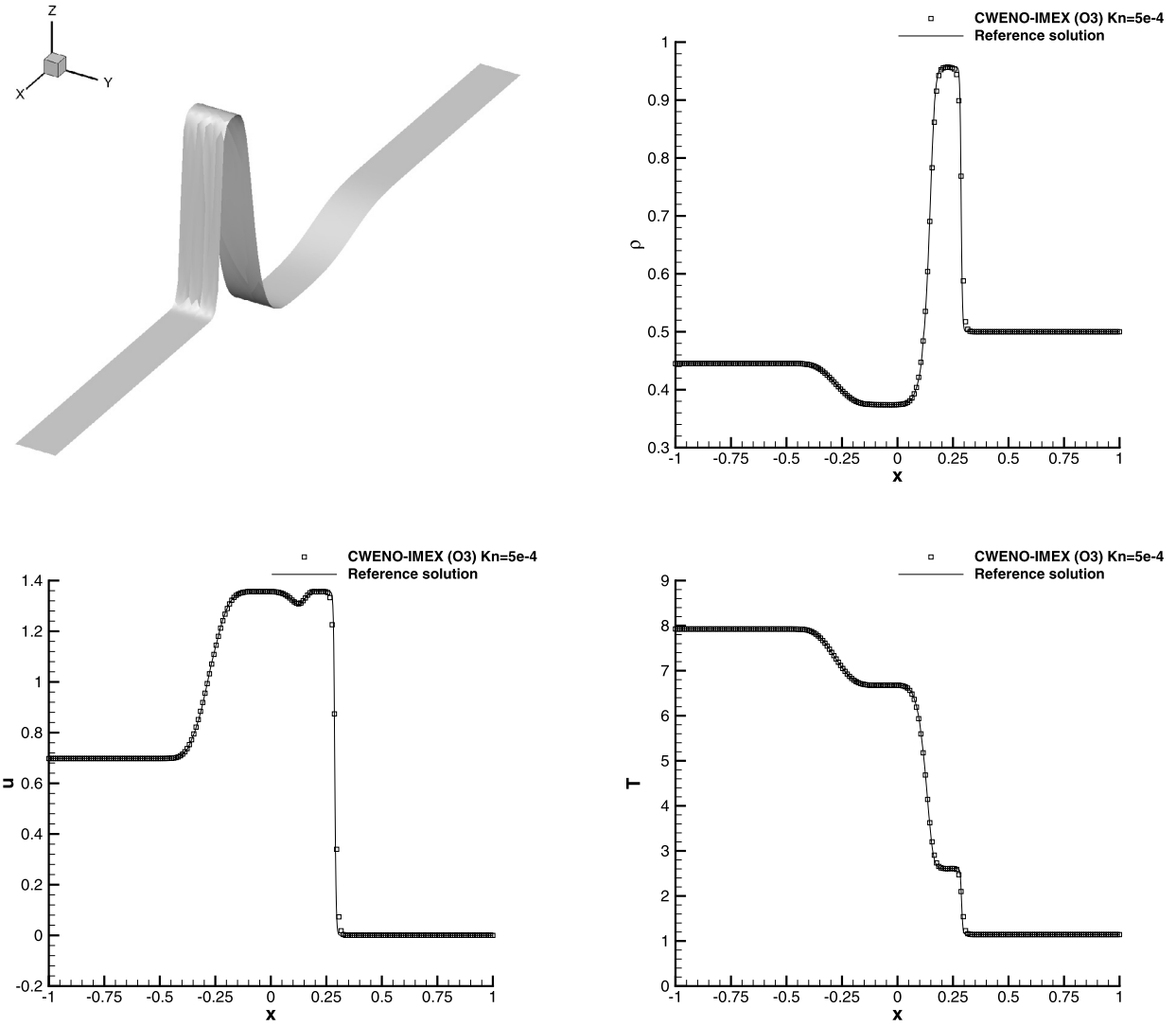

Fig. 7. Lax shock tube problem with $Kn = 5 \cdot 10^{-4}$ at time $t_f = 0.1$. Three dimensional view of density profile together with a 1D cut along the x-axis through the third order numerical results and comparison with exact solution for density, velocity in the x-direction and temperature.

Table 7
Simulation parameters: number of elements in the physical space N_p, number of elements in the velocity space N_v, polynomial degree of the spatial reconstruction M with associated degrees of freedom in space and time $(M+1)+\mathcal{M}(M)$ and total number of degrees of freedom $N_{dof} = N_p \cdot N_v \cdot ((M+1) \cdot \mathcal{M}(M))$ of the simulation.

Test problem	N_p	N_v	M	$(M+1)+\mathcal{M}(M)$	N_{dof}
Lax	1764	1024	2	9	16'257'024
Explosion	35186	1024	2	9	324'274'176
NACA	6554	1600	2	9	94'377'600

Table 7 contains some information regarding the simulation parameters of the test cases shown in this work, namely number of elements in the physical space N_p, number of elements in the velocity space N_v, polynomial degree of the spatial reconstruction M with associated degrees of freedom in space and time $(M+1)+\mathcal{M}(M)$ and total number of degrees of freedom $N_{dof} = N_p \cdot N_v \cdot ((M+1) \cdot \mathcal{M}(M))$ of the simulation. Here, we have performed simulations with up to ≈ 325 millions of degrees of freedom, which undoubtedly require an efficient parallelization strategy.

Finally, Table 8 collects the computational times referred to the main stages of the algorithm, that are as follows:

- CWENO reconstruction step (see Section 4.2);

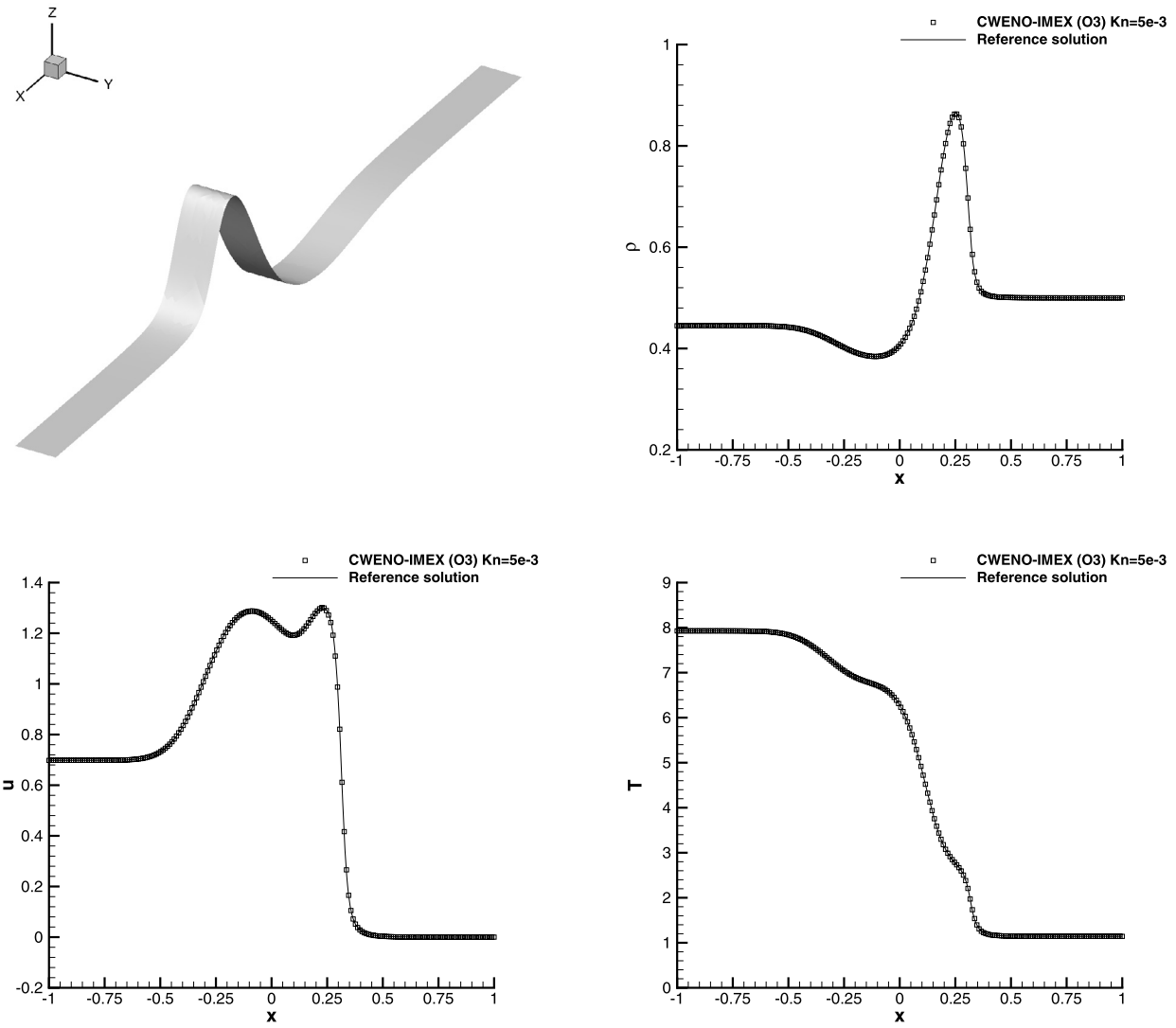

Fig. 8. Lax shock tube problem with $Kn = 5 \cdot 10^{-3}$ at time $t_f = 0.1$. Three dimensional view of density profile together with a 1D cut along the x-axis through the third order numerical results and comparison with exact solution for density, velocity in the x-direction and temperature.

- transport step in the finite volume scheme (39), i.e. evaluation of high order numerical fluxes across boundary cells given by the term $\sum_{j=1}^{N_{V_i}} \int_{\partial P_{i_j}} L(f_k^n) \cdot \; n_{ij}\, dS$;
- computation of the collision operator, including high order moments and volume integral, that is the term $\frac{\Delta t}{|P_i|} \times \int_{P_i} Q\,(f_k^n)\, dx$ in (39).

All simulations have been run in parallel on 128 Intel Xeon Gold processors with 256 GB of RAM. The evaluation of the numerical fluxes is the most expensive part of the algorithm that covers about 90% of the entire computational time, which is due to the high order integration based on Gaussian formulae and on the simplex splitting of the polygonal cells. This suggests to further investigate how to optimize the numerical integration across cell boundaries of arbitrary shaped closed control volumes. The CWENO reconstruction step also requires some computational resources as well as the evaluation of the collision operator, even though the latter is the part of the entire scheme which needs less computational resources.

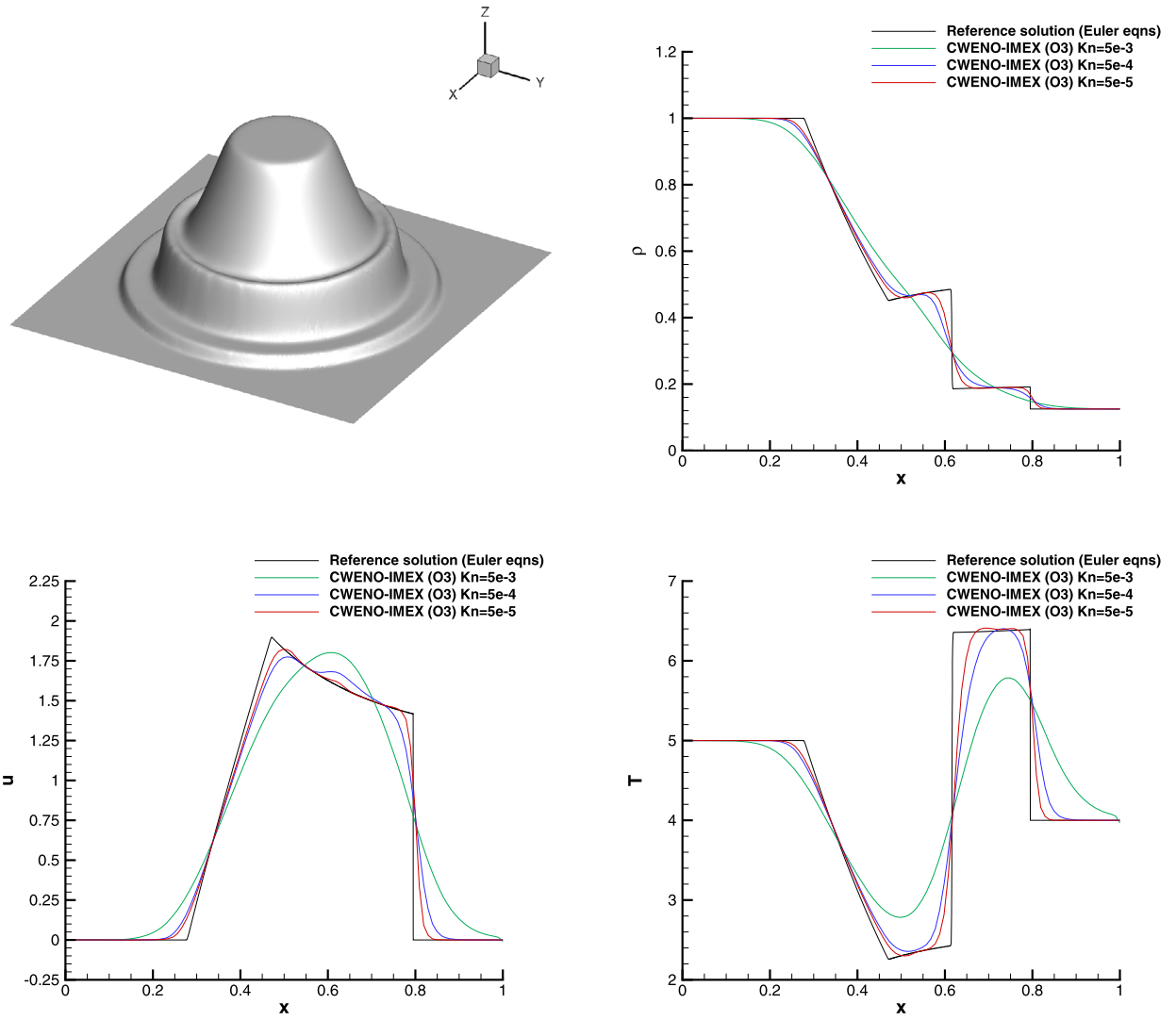

Fig. 9. Explosion problem with different Knudsen number, namely $Kn = 5 \cdot 10^{-5}$ (red line), $Kn = 5 \cdot 10^{-4}$ (blue line) and $Kn = 5 \cdot 10^{-3}$ (green line) at final time $t_f = 0.07$. Three dimensional view of density profile for the case with $Kn = 5 \cdot 10^{-5}$ (top left) is plot together with a 1D cut along the x-axis through the third order numerical results for density, horizontal velocity and temperature.

Table 8
Computational times in seconds [s] needed for the main steps of the algorithm: CWENO reconstruction stage, transport stage (evaluation of high order numerical fluxes across cell boundaries) and collision operator (evaluation of high order volume integral) in the finite volume scheme (39). Corresponding percentages w.r.t. the total computational time are given in brackets.

Test problem	Reconstruction	Transport	Collision operator
Lax ($Kn = 5 \cdot 10^{-3}$)	6'112 [$\approx$ 9.7 %]	56'344 [$\approx$ 89.6 %]	460 [$\approx$ 0.7 %]
Lax ($Kn = 5 \cdot 10^{-4}$)	6'055 [$\approx$ 9.6 %]	56'274 [$\approx$ 89.6 %]	474 [$\approx$ 0.8 %]
Lax ($Kn = 5 \cdot 10^{-5}$)	6'081 [$\approx$ 9.7 %]	56'403 [$\approx$ 89.6 %]	467 [$\approx$ 0.7 %]
Explosion ($Kn = 5 \cdot 10^{-3}$)	87'161 [$\approx$ 7.0 %]	1'145'428 [$\approx$ 92.2 %]	9'365 [$\approx$ 0.8 %]
Explosion ($Kn = 5 \cdot 10^{-4}$)	87'262 [$\approx$ 7.0 %]	1'145'314 [$\approx$ 92.2 %]	9'301 [$\approx$ 0.7 %]
Explosion ($Kn = 5 \cdot 10^{-5}$)	87'159 [$\approx$ 7.0 %]	1'147'199 [$\approx$ 92.2 %]	9'331 [$\approx$ 0.8 %]
NACA ($Kn = 1 \cdot 10^{-4}$, $\alpha = 0$)	109'333 [$\approx$ 4.0 %]	2'613'320 [$\approx$ 95.4 %]	16'659 [$\approx$ 0.6 %]
NACA ($Kn = 5 \cdot 10^{-3}$, $\alpha = 0$)	89'805 [$\approx$ 3.9 %]	2'202'802 [$\approx$ 95.5 %]	13'587 [$\approx$ 0.6 %]
NACA ($Kn = 1 \cdot 10^{-4}$, $\alpha = 20$)	110'707 [$\approx$ 3.9 %]	2'727'072 [$\approx$ 95.5 %]	16'775 [$\approx$ 0.6 %]
NACA ($Kn = 5 \cdot 10^{-3}$, $\alpha = 20$)	101'746 [$\approx$ 4.0 %]	2'430'181 [$\approx$ 95.4 %]	15'222 [$\approx$ 0.6 %]

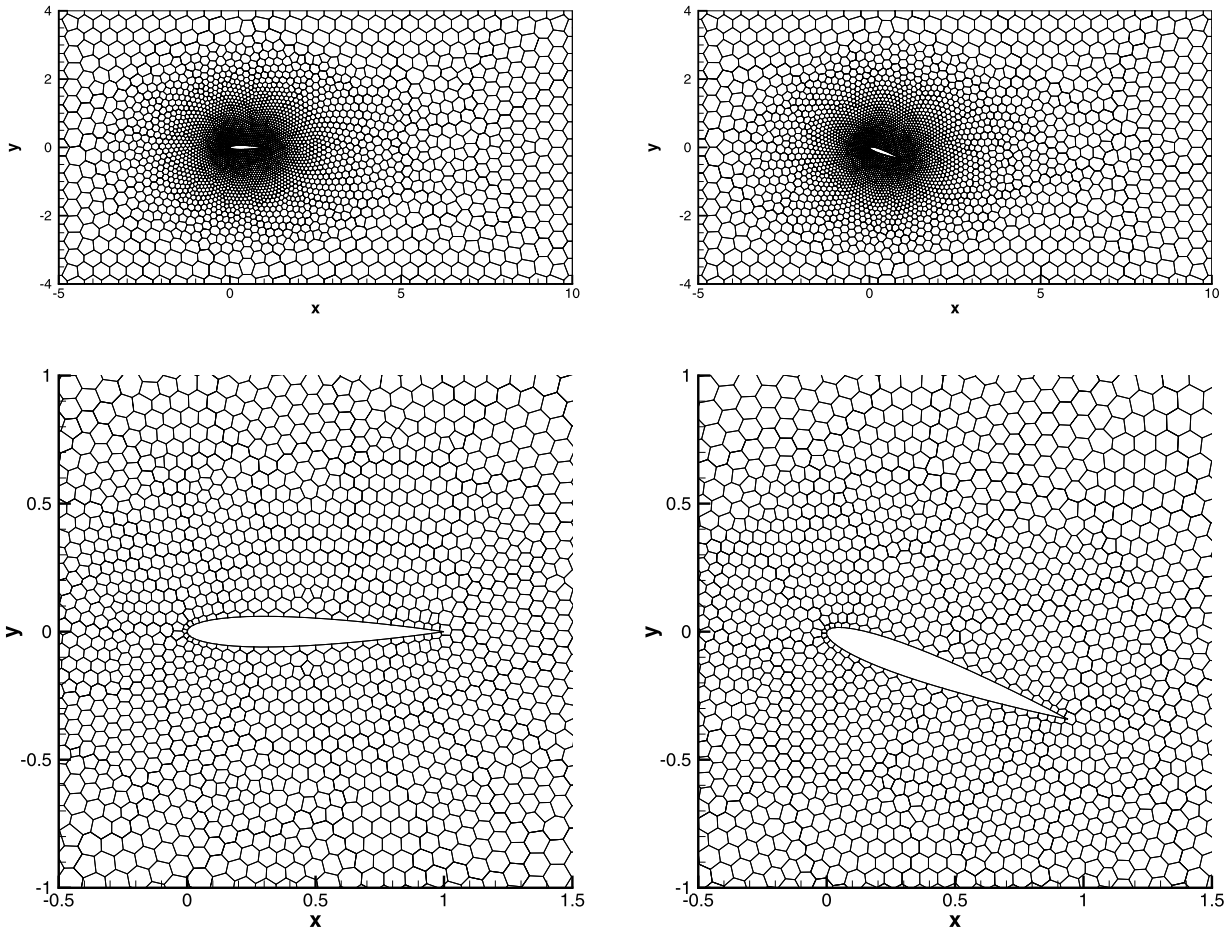

Fig. 10. Computational mesh used for the simulation of the flow around NACA 0012 airfoil with angle of attack $\alpha = 0$ (left) and $\alpha = 20$ (right). The computational domain is the box $\Omega = [-5; 10] \times [-4; 4]$ and it is discretized with a total number of Voronoi elements $N_E = 6518$ and $N_E = 6554$, respectively, with a characteristic mesh size $h = 0.5$. The airfoil profile has been approximated using 50 nodes. Zoom around the airfoil is shown in the bottom row.

7. Conclusions

In this work, we have presented a high order in space and time finite volume class of methods for solving the BGK kinetic equation on arbitrarily shaped elements in space. The method is based on a discrete ordinate approach for discretizing the velocity space, on a CWENO polynomial reconstruction in space on arbitrarily unstructured control volumes and on a Implicit-Explicit Runge-Kutta asymptotic preserving time discretization. The proposed IMEX schemes have been adapted to the finite volume framework and their properties in terms of asymptotic accuracy and preservation have been studied. Up to our knowledge, this is the first example in which such WENO reconstruction which enjoy the possibility of working with very small stencils is used for solving kinetic equations on unstructured meshes in a multidimensional setting. The flexibility due to the type of employed mesh together with the efficiency related to the polynomial reconstruction are of paramount importance when dealing with realistic simulations which use kinetic equations, due to the intrinsic computational complexity of these models. All these technologies are combined with the more advanced state of the art concerning the time discretization of kinetic models in stiff regimes guaranteeing stability, accuracy and preservation of the asymptotic state to the full scheme.

In the numerical part, we tested the methods verifying that the theoretical order of convergence is indeed guaranteed by our schemes for different flow regimes from dense to rarefied fluids. A set of benchmark problems are also reported showing the capability and the robustness of the schemes, and a more realistic simulation which is not possible to perform on regular structured grids is run on a MPI parallelization of our code providing evidence that our approach can be applied for large scale simulations as well. Profiling analysis and simulation details have finally been provided at the end of the paper, resuming the computational resources needed by each main step of the algorithm.

In the future, we would like to extend the methods here presented in several directions. We intend to work on the full three dimensional case, to increase the time precision by using linear multistep approaches which allow to reach up to fifth

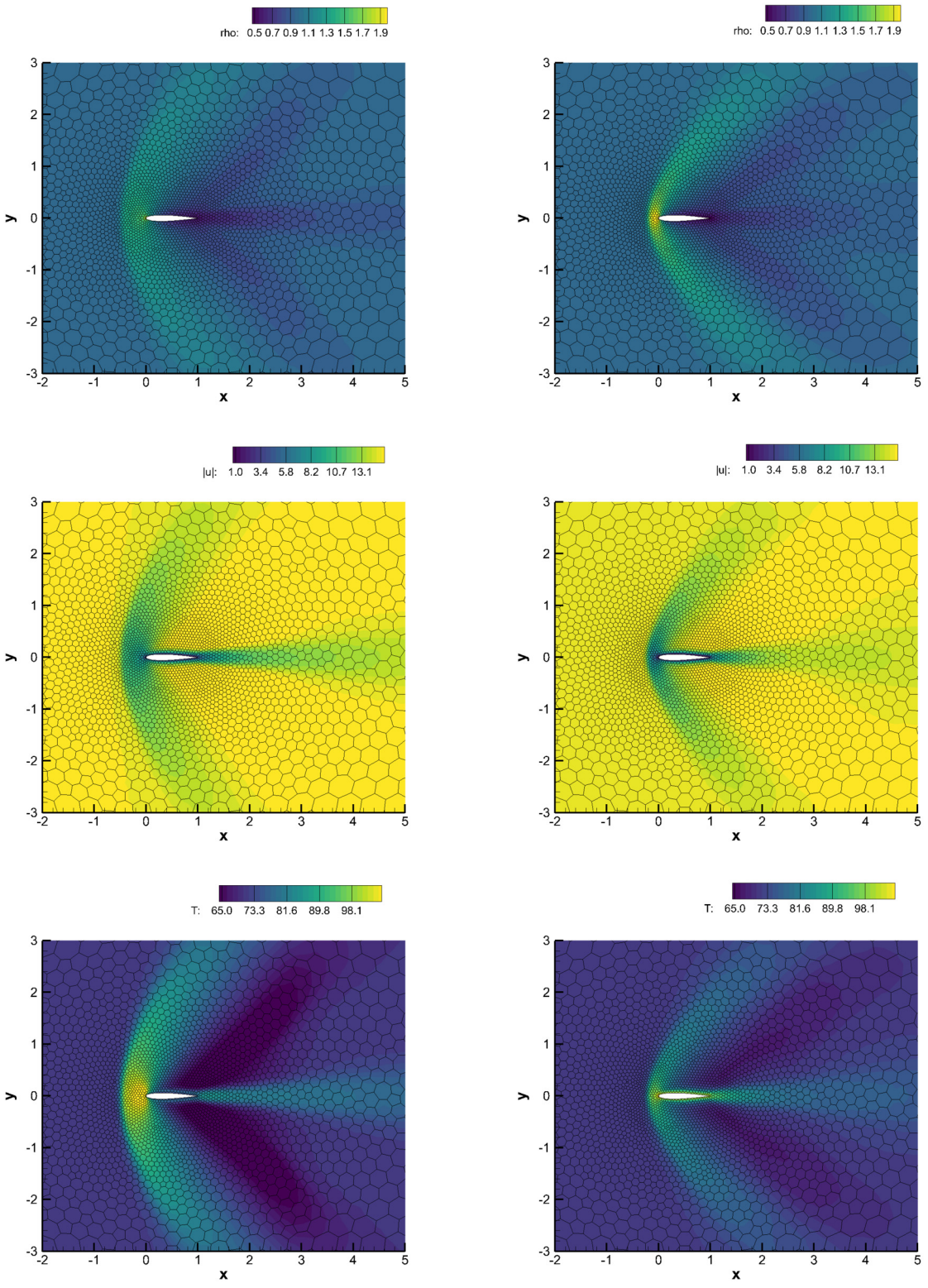

Fig. 11. Numerical results at time $t = 0.5$ with airfoil angle $\alpha = 0$ with third order CWENO-IMEX for BGK with $\varepsilon_1 = 10^{-4}$ (left column) and with third order CWENO-ADER for Navier-Stokes with $\mu_1 = 7.142857 \cdot 10^{-3}$ (right column). Density (top row), magnitude of the velocity field (middle row) and temperature (bottom row) are displayed.

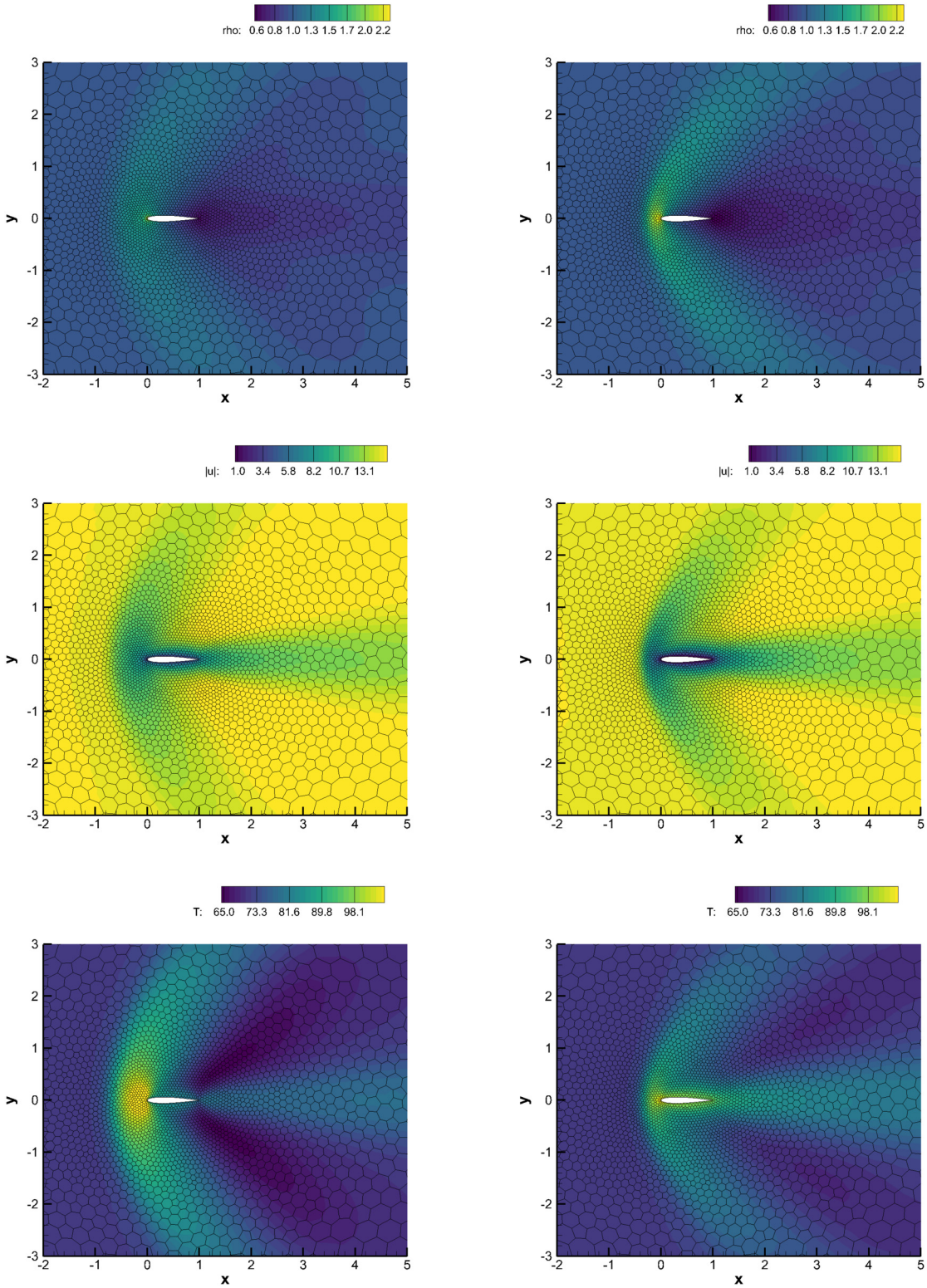

Fig. 12. Numerical results at time $t = 0.5$ with airfoil angle $\alpha = 0$ with third order CWENO-IMEX for BGK with $\varepsilon_1 = 5 \cdot 10^{-3}$ (left column) and with third order CWENO-ADER for Navier-Stokes with $\mu_1 = 3.571459 \cdot 10^{-1}$ (right column). Density (top row), magnitude of the velocity field (middle row) and temperature (bottom row) are displayed.

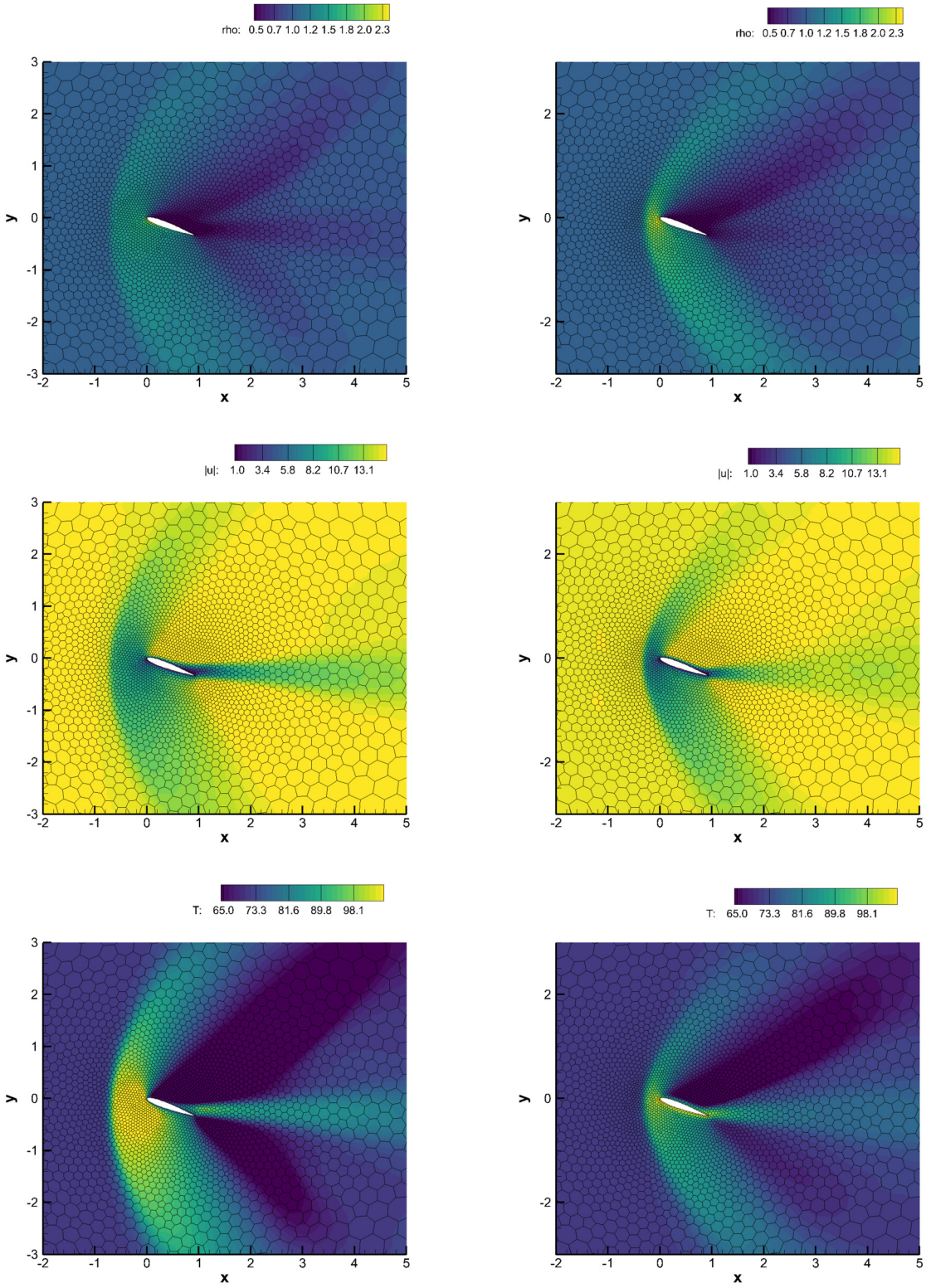

Fig. 13. Numerical results at time $t = 0.5$ with airfoil angle $\alpha = 20$ with third order CWENO-IMEX for BGK with $\varepsilon_1 = 10^{-4}$ (left column) and with third order CWENO-ADER for Navier-Stokes with $\mu_1 = 7.142857 \cdot 10^{-3}$ (right column). Density (top row), magnitude of the velocity field (middle row) and temperature (bottom row) are displayed.

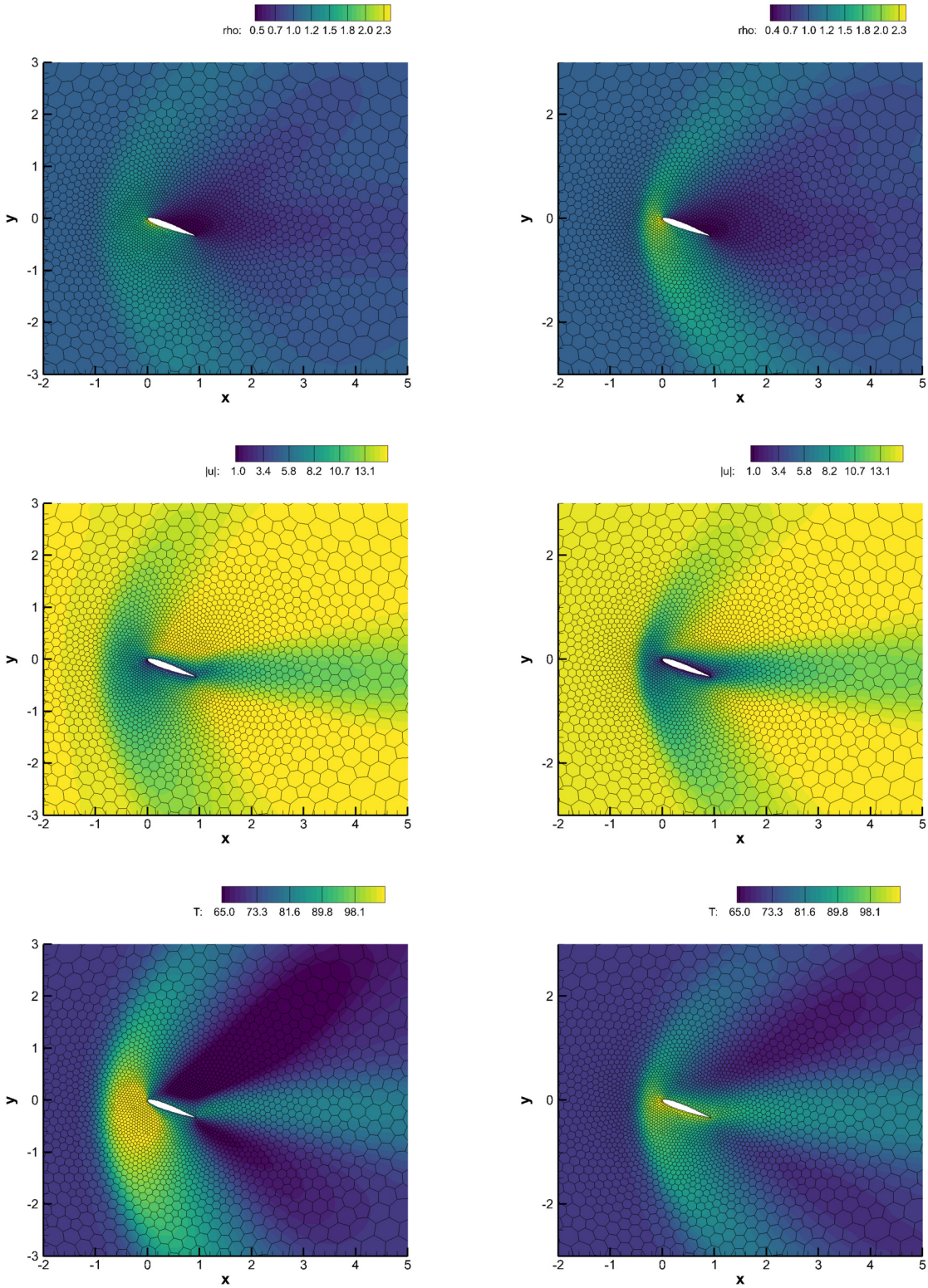

Fig. 14. Numerical results at time $t = 0.5$ with airfoil angle $\alpha = 20$ with third order CWENO-IMEX for BGK with $\varepsilon_1 = 5 \cdot 10^{-3}$ (left column) and with third order CWENO-ADER for Navier-Stokes with $\mu_1 = 3.571459 \cdot 10^{-1}$ (right column). Density (top row), magnitude of the velocity field (middle row) and temperature (bottom row) are displayed.

order of accuracy in time. We want also to consider arbitrarily shaped grids in velocity space and to deal with more realistic kinetic models such as the full Boltzmann operator. An interesting direction of research consists also in using such method to perform a detailed study of the flow around airfoils employing kinetic models.

CRediT authorship contribution statement

Walter Boscheri: conceptualization, implementation, computation.
Giacomo Dimarco: conceptualization, lemma and proofs, writing.

Declaration of competing interest

The authors declare that they have no known competing financial interests or personal relationships that could have appeared to influence the work reported in this paper.

Acknowledgements

The Authors would like to thank the Italian Ministry of Instruction, University and Research (MIUR) to support this research with funds coming from PRIN Project 2017 (No. 2017KKJP4X entitled "Innovative numerical methods for evolutionary partial differential equations and applications"). W.B. has been partially financed by INdAM (Italian National Institute of High Mathematics) under the program *Young researchers funding 2018*. The Authors acknowledge the Italian Super-Computing Resource Allocation (ISCRA) for awarding them access to the MARCONI supercomputer based in Bologna (Italy), under the project *IscrC_HiPPUM_0*. Special thanks to Prof. Michael Dumbser (University of Trento) for granting access to the *STiMulUs* AMD Opteron cluster, which has been used to produce some results shown in this article.

References

[1] R. Abgrall, On essentially non-oscillatory schemes on unstructured meshes: analysis and implementation, J. Comput. Phys. 144 (1994) 45–58.
[2] Abgrall Remi, A review of residual distribution schemes for hyperbolic and parabolic problems: the July 2010 state of the art, Commun. Comput. Phys. 11 (4) (2012) 1043–1080.
[3] U.M. Ascher, S.J. Ruuth, R.J. Spiteri, Implicit-explicit Runge-Kutta methods for time-dependent partial differential equations, Appl. Numer. Math. 25 (2–3) (1997) 151–167, Special Issue on Time Integration (Amsterdam, 1996).
[4] L.L. Baker, N.G. Hadjiconstantinou, Variance-reduced Monte Carlo solutions of the Boltzmann equation for low-speed gas flows: a discontinuous Galerkin formulation, Int. J. Numer. Methods Fluids 58 (4) (2008) 381–402.
[5] C. Baranger, J. Claudel, N. Hérouard, L. Mieussens, Locally refined discrete velocity grids for stationary rarefied flow simulations, J. Comput. Phys. 257 (part A) (2014) A:572–593.
[6] T.J. Barth, P.O. Frederickson, Higher order solution of the Euler equations on unstructured grids using quadratic reconstruction, 28th Aerospace Sciences Meeting, AIAA paper no. 90-0013, January 1990.
[7] T.J. Barth, D.C. Jespersen, The design and application of upwind schemes on unstructured meshes, AIAA Paper 89-0366, 1989, pp. 1–12.
[8] M. Bennoune, M. Lemou, L. Mieussens, Uniformly stable numerical schemes for the Boltzmann equation preserving the compressible Navier-Stokes asymptotics, J. Comput. Phys. 227 (2008) 3781–3803.
[9] P.L. Bhatnagar, E.P. Gross, M. Krook, A model for collision processes in gases. I. Small amplitude processes in charged and neutral one-component systems, Phys. Rev. 94 (3) (1954) 511–525.
[10] G.A. Bird, Molecular Gas Dynamics and the Direct Simulation of Gas Flows, 2nd edition, Oxford University Press, 1994.
[11] A.V. Bobylev, A. Palczewski, J. Schneider, On approximation of the Boltzmann equation by discrete velocity models, C. R. Acad. Sci., Sér. 1 Math. 320 (5) (1995) 639–644.
[12] S. Boscarino, L. Pareschi, G. Russo, Implicit-explicit Runge-Kutta schemes for hyperbolic systems and kinetic equations in the diffusion limit, SIAM J. Sci. Comput. 35 (2013) A22–A51.
[13] S. Boscarino, G. Russo, M. Semplice, High order finite volume schemes for balance laws with stiff relaxation, Comput. Fluids 169 (2018) 155–168.
[14] W. Boscheri, M. Dumbser, Arbitrary–Lagrangian–Eulerian one–step WENO finite volume schemes on unstructured triangular meshes, Commun. Comput. Phys. 14 (2013) 1174–1206.
[15] A. Bowyer, Computing Dirichlet tessellations, Comput. J. 24 (2) (1981) 162–166.
[16] Henri Cabannes, Renée Gatignol, Li-Shi Luo, The Discrete Boltzmann Equation (Theory and Applications), Henri Cabannes, Paris, 2003.
[17] R.E. Caflisch, Monte Carlo and quasi-Monte Carlo methods, Acta Numer. 7 (1998) 1–49.
[18] C. Cercignani, The Boltzmann Equation and Its Applications, Applied Mathematical Sciences, vol. 67, Springer-Verlag, New York, 1988.
[19] S. Chapman, D. Burnett, T.G. Cowling, The Mathematical Theory of Non-uniform Gases, Cambridge University Press, Cambridge, 1970.
[20] C.Z. Cheng, G. Knorr, The integration of the Vlasov equation in configuration space, J. Comput. Phys. 22 (1976) 330–351.
[21] B. Cockburn, C. Johnson, C.W. Shu, E. Tadmor, Essentially non-oscillatory and weighted essentially non-oscillatory schemes for hyperbolic conservation laws, in: A. Quarteroni (Ed.), Advanced Numerical Approximation of Nonlinear Hyperbolic Equations, in: Lecture Notes in Mathematics, vol. 1697, Springer, 1998, pp. 325–432.
[22] I. Cravero, G. Puppo, M. Semplice, G. Visconti, Cool WENO schemes, Comput. Fluids 169 (2018) 71–86.
[23] I. Cravero, G. Puppo, M. Semplice, G. Visconti, CWENO: uniformly accurate reconstructions for balance laws, Math. Comp. 87 (2018) 1689–1719.
[24] I. Cravero, M. Semplice, On the accuracy of WENO and CWENO reconstructions of third order on nonuniform meshes, J. Sci. Comput. 67 (2016) 1219–1246.
[25] N. Crouseilles, G. Dimarco, M. Lemou, Asymptotic preserving and time diminishing schemes for rarefied gas dynamic, Kinet. Relat. Models 10 (3) (2017) 643–668.
[26] N. Crouseilles, M. Lemou, F. Méhats, Asymptotic preserving schemes for highly oscillatory Vlasov-Poisson equations, J. Comput. Phys. 248 (2013) 287–308.
[27] N. Crouseilles, M. Mehrenberger, E. Sonnendrücker, Conservative semi-Lagrangian schemes for Vlasov equations, J. Comput. Phys. 229 (6) (2010) 1927–1953.

[28] N. Crouseilles, T. Respaud, E. Sonnendrücker, A forward semi-Lagrangian method for the numerical solution of the Vlasov equation, Comput. Phys. Commun. 180 (10) (2009) 1730–1745.
[29] G. Dechristé, L. Mieussens, A Cartesian cut cell method for rarefied flow simulations around moving obstacles, J. Comput. Phys. 314 (2016) 465–488.
[30] P. Degond, Asymptotic-Preserving Schemes for Fluid Models of Plasmas, Panoramas et Syntheses, SMF, 2014.
[31] P. Degond, F. Deluzet, Asymptotic-preserving methods and multiscale models for plasma physics, J. Comput. Phys. 336 (2017) 429–457.
[32] P. Degond, F. Deluzet, L. Navoret, A.-B. Sun, M.-H. Vignal, Asymptotic-preserving particle-in-cell method for the Vlasov-Poisson system near quasineutrality, J. Comput. Phys. 229 (16) (2010) 5630–5652.
[33] G. Dimarco, The moment guided Monte Carlo method for the Boltzmann equation, Kinet. Relat. Models 6 (2) (2013) 291–315.
[34] G. Dimarco, R. Loubère, Towards an ultra efficient kinetic scheme. Part I: basics on the BGK equation, J. Comput. Phys. 255 (2013) 680–698.
[35] G. Dimarco, R. Loubère, Towards an ultra efficient kinetic scheme. Part II: the high order case, J. Comput. Phys. 255 (2013) 699–719.
[36] G. Dimarco, R. Loubère, J. Narski, Towards an ultra efficient kinetic scheme. Part III: high-performance-computing, J. Comput. Phys. 284 (2015) 22–39.
[37] G. Dimarco, Raphaël Loubère, Jacek Narski, Thomas Rey, An efficient numerical method for solving the Boltzmann equation in multidimensions, J. Comput. Phys. 353 (2018) 46–81.
[38] G. Dimarco, L. Pareschi, Hybrid multiscale methods. II. Kinetic equations, Multiscale Model. Simul. 6 (4) (2007/2008) 1169–1197.
[39] G. Dimarco, L. Pareschi, Fluid solver independent hybrid methods for multiscale kinetic equations, SIAM J. Sci. Comput. 32 (2) (2010) 603–634.
[40] G. Dimarco, L. Pareschi, Exponential Runge-Kutta methods for stiff kinetic equations, SIAM J. Numer. Anal. 49 (5) (2011) 2057–2077.
[41] G. Dimarco, L. Pareschi, High order asymptotic-preserving schemes for the Boltzmann equation, C. R. Math. Acad. Sci. Paris 350 (9–10) (2012) 481–486.
[42] G. Dimarco, L. Pareschi, Asymptotic preserving implicit-explicit Runge-Kutta methods for nonlinear kinetic equations, SIAM J. Numer. Anal. 51 (2) (2013) 1064–1087.
[43] G. Dimarco, L. Pareschi, Numerical methods for kinetic equations, Acta Numer. 23 (2014) 369–520.
[44] G. Dimarco, L. Pareschi, Implicit-explicit linear multistep methods for stiff kinetic equations, SIAM J. Numer. Anal. 55 (2) (2017) 664–690.
[45] M. Dumbser, W. Boscheri, M. Semplice, G. Russo, Central weighted ENO schemes for hyperbolic conservation laws on fixed and moving unstructured meshes, SIAM J. Sci. Comput. 39 (6) (2017) A2564–A2591.
[46] M. Dumbser, C. Enaux, E.F. Toro, Finite volume schemes of very high order of accuracy for stiff hyperbolic balance laws, J. Comput. Phys. 227 (2008) 3971–4001.
[47] M. Dumbser, M. Kaeser, Arbitrary high order non-oscillatory finite volume schemes on unstructured meshes for linear hyperbolic systems, J. Comput. Phys. 221 (2007) 693–723.
[48] M. Dumbser, M. Kaeser, V.A. Titarev, E.F. Toro, Quadrature-free non-oscillatory finite volume schemes on unstructured meshes for nonlinear hyperbolic systems, J. Comput. Phys. 226 (2007) 204–243.
[49] M. Dumbser, O. Zanotti, A. Hidalgo, D.S. Balsara, ADER-WENO finite volume schemes with space-time adaptive mesh refinement, J. Comput. Phys. 248 (2013) 257–286.
[50] F. Filbet, E. Sonnendrücker, P. Bertrand, Conservative numerical schemes for the Vlasov equation, J. Comput. Phys. 172 (1) (September 2001) 166–187.
[51] F. Filbet, S. Jin, A class of asymptotic-preserving schemes for kinetic equations and related problems with stiff sources, J. Comput. Phys. 229 (20) (2010) 7625–7648.
[52] F. Filbet, G. Russo, High order numerical methods for the space non-homogeneous Boltzmann equation, J. Comput. Phys. 186 (2) (April 2003) 457–480.
[53] F. Filbet, G. Russo, Accurate numerical methods for the Boltzmann equation, in: Modeling and Computational Methods for Kinetic Equations, Springer, 2004, pp. 117–145.
[54] Francis Filbet, Thomas Rey, A rescaling velocity method for dissipative kinetic equations. Applications to granular media, J. Comput. Phys. 248 (2013) 177–199.
[55] Elena Gaburro, Walter Boscheri, Simone Chiocchetti, Christian Klingenberg, Volker Springel, Michael Dumbser, High order direct arbitrary-Lagrangian-Eulerian schemes on moving Voronoi meshes with topology changes, J. Comput. Phys. 407 (2020) 109167.
[56] I.M. Gamba, S.H. Tharkabhushanam, Spectral-Lagrangian methods for collisional models of non-equilibrium statistical states, J. Comput. Phys. 228 (6) (April 2009) 2012–2036.
[57] S.K. Godunov, A.V. Zabrodin, G.P. Prokopov, A difference scheme for two-dimensional unsteady aerodynamics, USSR Comput. Math. Math. Phys. 2 (6) (1961) 1020–1050.
[58] M. Groppi, G. Russo, G. Stracquadanio, High order semi-Lagrangian methods for the BGK equation, Commun. Math. Sci. 14 (2) (2016) 389–414.
[59] Lowell H. Holway Jr., Kinetic theory of shock structure using an ellipsoidal distribution function, in: Rarefied Gas Dynamics, vol. I, Proc. Fourth Internat. Sympos., Univ. Toronto, 1964, Academic Press, New York, 1966, pp. 193–215.
[60] C. Hu, C.W. Shu, A high-order weno finite difference scheme for the equations of ideal magnetohydrodynamics, J. Comput. Phys. 150 (1999) 561–594.
[61] C. Hu, C.W. Shu, Weighted essentially non-oscillatory schemes on triangular meshes, J. Comput. Phys. 150 (1999) 97–127.
[62] J. Hu, R. Shu, X. Zhang, Asymptotic-preserving and positivity-preserving implicit-explicit schemes for the stiff BGK equation, SIAM J. Numer. Anal. 56 (2) (2018) 942–973.
[63] J. Hu, X. Zhang, On a class of implicit-explicit Runge-Kutta schemes for stiff kinetic equations preserving the Navier-Stokes limit, J. Sci. Comput. 73 (2–3) (2017) 797–818.
[64] J.-C. Huang, K. Xu, P. Yu, A unified gas-kinetic scheme for continuum and rarefied flows II: multi-dimensional cases, Commun. Comput. Phys. 12 (3) (2012) 662–690.
[65] Florence Hubert, Rémi Tesson, Weno scheme for transport equation on unstructured grids with a DDFV approach, in: Finite Volumes for Complex Applications VIII—Hyperbolic, Elliptic and Parabolic Problems, in: Springer Proc. Math. Stat., vol. 200, Springer, Cham, 2017, pp. 13–21.
[66] G.-S. Jiang, C.W. Shu, Efficient implementation of weighted ENO schemes, J. Comput. Phys. 126 (1996) 202–228.
[67] G.S. Jiang, C.W. Shu, Efficient implementation of weighted eno schemes, J. Comput. Phys. (1996) 202–228.
[68] S. Jin, Efficient asymptotic-preserving (ap) schemes for some multiscale kinetic equations, SIAM J. Sci. Comput. 21 (1999) 441–454.
[69] S. Jin, Asymptotic preserving (AP) schemes for multiscale kinetic and hyperbolic equations: a review, Riv. Mat. Univ. Parma 3 (2) (2012) 177–216.
[70] J. Zhu, X. Zhong, C.W. Shu, J. Qiu, Runge-Kutta discontinuous Galerkin method using a new type of weno limiters on unstructured meshes, J. Comput. Phys. 248 (2013) 200–220.
[71] G. Karypis, V. Kumar, Multilevel k-way partitioning scheme for irregular graphs, J. Parallel Distrib. Comput. 48 (1998) 96–129.
[72] M. Käser, A. Iske, ADER schemes on adaptive triangular meshes for scalar conservation laws, J. Comput. Phys. 205 (2005) 486–508.
[73] D. Levy, G. Puppo, G. Russo, Central WENO schemes for hyperbolic systems of conservation laws, Modél. Math. Anal. Numér. 33 (3) (1999) 547–571.
[74] D. Levy, G. Puppo, G. Russo, Compact central WENO schemes for multidimensional conservation laws, SIAM J. Sci. Comput. 22 (2) (2000) 656–672.
[75] Q. Li, L. Pareschi, Exponential Runge-Kutta for the inhomogeneous Boltzmann equations with high order of accuracy, J. Comput. Phys. 259 (2014) 402–420.
[76] Q. Li, X. Yang, Exponential Runge-Kutta methods for the multispecies Boltzmann equation, Commun. Comput. Phys. 15 (4) (2014) 996–1011.
[77] C. Liu, K. Xu, Q. Sun, Q. Cai, A unified gas-kinetic scheme for continuum and rarefied flows IV: full Boltzmann and model equations, J. Comput. Phys. 314 (2016) 305–340.
[78] L. Mieussens, Discrete velocity model and implicit scheme for the BGK equation of rarefied gas dynamics, Math. Models Methods Appl. Sci. 10 (08) (2000) 1121–1149.

[79] Clément Mouhot, Lorenzo Pareschi, Thomas Rey, Convolutive decomposition and fast summation methods for discrete-velocity approximations of the Boltzmann equation, ESAIM: Math. Model. Numer. Anal. 47 (5) (2013) 1515–1531.
[80] K. Nanbu, Direct simulation scheme derived from the Boltzmann equation. I. Monocomponent gases, J. Phys. Soc. Jpn. 49 (5) (1980) 2042–2049.
[81] A. Palczewski, J. Schneider, Existence, stability, and convergence of solutions of discrete velocity models to the Boltzmann equation, J. Stat. Phys. 91 (1–2) (1998) 307–326.
[82] A. Palczewski, J. Schneider, Alexandre V. Bobylev, A consistency result for a discrete-velocity model of the Boltzmann equation, SIAM J. Numer. Anal. 34 (5) (1997) 1865–1883.
[83] L. Pareschi, G. Russo, Implicit-explicit Runge-Kutta schemes and applications to hyperbolic systems with relaxation, J. Sci. Comput. 25 (1–2) (2005) 129–155.
[84] S. Pieraccini, G. Puppo, Implicit–explicit schemes for BGK kinetic equations, J. Sci. Comput. 32 (1) (2007) 1–28.
[85] Tadeusz Płatkowski, Reinhard Illner, Discrete velocity models of the Boltzmann equation: a survey on the mathematical aspects of the theory, SIAM Rev. 30 (2) (1988) 213–255.
[86] V.V. Rusanov, Calculation of interaction of non-steady shock waves with obstacles, USSR Comput. Math. Math. Phys. 1 (1961) 267–279.
[87] M. Semplice, A. Coco, G. Russo, Adaptive mesh refinement for hyperbolic systems based on third-order compact WENO reconstruction, J. Sci. Comput. 66 (2) (2016) 692–724.
[88] C.-W. Shu, Essentially non-oscillatory and weighted essentially non-oscillatory schemes for hyperbolic conservation laws, in: Advanced Numerical Approximation of Nonlinear Hyperbolic Equations, Springer, 1998, pp. 325–432.
[89] A.H. Stroud, Approximate Calculation of Multiple Integrals, Prentice-Hall Inc., Englewood Cliffs, New Jersey, 1971.
[90] V. Titarev, M. Dumbser, S. Utyuzhnikov, Construction and comparison of parallel implicit kinetic solvers in three spatial dimensions, J. Comput. Phys. 256 (2014) 17–33.
[91] V.A. Titarev, Conservative numerical methods for model kinetic equations, Comput. Fluids 36 (9) (2007) 1446–1459.
[92] V.A. Titarev, E.F. Toro, Finite-volume WENO schemes for three-dimensional conservation laws, J. Comput. Phys. 201 (1) (2004) 238–260.
[93] E.F. Toro, Riemann Solvers and Numerical Methods for Fluid Dynamics: A Practical Introduction, Springer, 2009.
[94] T. Xiong, J. Jang, F. Li, J.-M. Qiu, High order asymptotic preserving nodal discontinuous Galerkin IMEX schemes for the BGK equation, J. Comput. Phys. 284 (2015) 70–94.
[95] T. Xiong, J.-M. Qiu, A hierarchical uniformly high order DG-IMEX scheme for the 1D BGK equation, J. Comput. Phys. 336 (2017) 164–191.
[96] Y.T. Zhang, C.W. Shu, Third order WENO scheme on three dimensional tetrahedral meshes, Commun. Comput. Phys. 5 (2009) 836–848.